Paradoxical non-catalytic kinase functions are driven by inhibitor-induced displacement of autoinhibitory domains

Viviane Reber (1), Sabrina Keller (1), Stefanie A. Loosli (1), Yumi Arima (2), Tatjana Kleele (2), Paola Picotti (1), Matthias Gstaiger *(1)

1 Institute of Molecular Systems Biology, Department of Biology, ETH Zurich, Zurich, Switzerland
2 Institute of Biochemistry, Department of Biology, ETH Zurich, Zurich, Switzerland

* Corresponding author: Matthias Gstaiger, matthias.gstaiger@imsb.biol.ethz.ch

Abstract

ATP competitive kinase inhibitors represent one of the largest classes of targeted anti-cancer drugs. While their primary mechanism is to block catalytic activity, they can also trigger paradoxical phenotypic effects that cannot be explained by catalytic inhibition alone. These observations point to a hidden layer of drug action that modulates non-catalytic kinase functions via changes in kinase conformation and protein-protein interactions (PPIs). Here we developed a multimodal proteomics approach combining limited proteolysis coupled mass spectrometry on affinity purified samples (AP-LiP-MS), AP-MS, and proximity labeling-MS to map inhibitor-induced conformation and PPI changes. We show that inhibitor binding causes structural rearrangements in the AIDs of all tested kinases, consistent with a transition to an open, active-like kinase conformation. These structural shifts drive distinct kinase-protein interaction changes that control non-catalytic functions: sequestration of AMPK by inhibited CAMKK2 blocks phosphorylation by other kinases, CHEK1 inhibition causes dissociation from the mitochondrial protein CLPB and leads to mitochondrial fragmentation, and structural changes in inhibited PRKCA trigger rapid relocalization to cell junctions. Thus we identify the ATP-binding site as a major organizing center of kinase conformation and interaction. Our work suggests that these on-target, off-mechanism effects are highly prevalent and provides the analytical framework to systematically characterize a frequently overlooked phenomenon highly relevant for understanding drug side effects to guide the development of novel therapeutics.

Introduction

Most human proteins are phosphorylated by the 518 kinases[1], representing a key mechanism to organize the dynamic functional landscape of the proteome orchestrating the majority of cellular processes. Consequently, mutations and changes in signaling context that affect kinase function are often causally linked to the development of human diseases such as cancer[2,3]. Therapeutic efforts to correct aberrant kinase activity focused on the development of compounds which bind the kinase

33 domain (KD) and inhibit its catalytic activity. This resulted in a set of chemical probes targeting over
34 130 kinases[4]. Most probes targeting kinases inhibit their catalytic activity in an ATP-competitive
35 manner (also referred to as a type I inhibitor), representing one of the largest classes of FDA approved
36 anti-cancer drugs[5,6].
37 Classical target engagement analyses typically focus on kinetic parameters of catalytic inhibition, target
38 specificity and structural characterization of the probe-KD interaction. However, beyond the catalytic
39 core, protein kinases contain multiple additional domains that confer diverse biochemical functions
40 such as autoinhibition[7], subcellular localization, enzymatic activities or complex formation[8,9].
41 Understanding how inhibitors allosterically control such non-catalytic kinase functions is however key
42 to understanding drug action and toxicity.
43 The KD of most kinases consists of conserved structural elements which constitute a conformational
44 switch toggling between an active and inactive state. Human kinases are regulated via autoinhibitory
45 domains (AIDs) which, in the absence of activating signals, keep kinases in an inactive state by binding
46 to the KD and masking ATP binding site[10], controlling the accessibility and conformation of the ATP-
47 binding domain blocking both kinase activity and interactions with substrates[11,12]. Type I inhibitors
48 stabilize the active state of the KD, also called the aspartate-phenylalanine-glycine (DFG)-in
49 conformation. However, it remains unclear whether this active state also involves structural changes
50 at the AID, since the probe might not bind the autoinhibited state where the AID also binds at the
51 active site. This lack of data can be explained by the fact that structural changes in AID domains are
52 difficult to characterize by classical structural methods as many AIDs are disordered[13,14] or linked to
53 the KD via a disordered linker[15]. Therefore, it is plausible that a large fraction of kinases may undergo
54 larger domain-domain interaction and subsequent contextual changes in response to ATP-competitive
55 inhibitor binding. Consequently, while the biochemical and cellular consequences resulting from
56 inhibited substrate phosphorylation have been studied in great detail, the extent to which inhibitor-
57 induced open conformations govern cellular drug phenotypes remains a major dark space in kinome
58 pharmacology.
59 To bridge this gap and systematically discover such mechanisms, we combined structural and
60 contextual proteomics and applied it to three disease associated kinases regulated by AIDs for which
61 highly specific ATP competitive inhibitors were available: Calcium/calmodulin-dependent protein
62 kinase kinase 2 (CAMKK2), Checkpoint kinase 1 (CHEK1), and Protein kinase C alpha (PRKCA). To resolve
63 structural changes induced by ligand binding at high sequence coverage we employed limited
64 proteolysis coupled with mass spectrometry (LiP-MS) on native affinity purified (AP) samples (AP-LiP-
65 MS). We combined AP-LiP-MS with contextual proteomics, using both AP-MS[9] and *in vivo* proximity
66 labeling[16] as complementary approaches[17] to understand how inhibitor induced conformational shifts
67 reshape the kinase's interactome and biochemical environment. The combination of these methods

68 provides detailed insights on structural and protein-protein interaction (PPI) changes in response to
69 inhibitors without relying on prior knowledge and represents a generalizable and unbiased approach
70 that guides the *de novo* discovery of mechanisms of action.
71 Using our approach we identified a structural mechanism shared across all three kinases where
72 inhibitor binding displaces the AID inducing an active-like kinase conformation. This open but
73 catalytically inhibited state triggers novel molecular and cellular phenotypes, such as complex
74 remodelling, sequestration of proteins away from pathways or changes in protein localization. Our
75 findings suggest that inhibitor-induced neomorphic functions may represent a prevalent feature
76 among kinases with AIDs, establishing our multimodal proteomic strategy as a systematic roadmap to
77 identify off-mechanism liabilities for the development of safer, more effective kinase-targeted
78 therapeutics and probes.

79 Results

80 ATP-competitive kinase inhibition displaces the autoinhibitory domain to induce an 81 open conformation

82 To investigate probe-induced conformational changes in flexible protein regions, we used LiP-MS[18], a
83 structural proteomics method that relies on the generation of conformation specific protein fragments
84 by the protease proteinase K (PK), which preferentially cleaves accessible and flexible regions[19].
85 Perturbations that alter protein accessibility or flexibility lead to changes in PK cleavage patterns,
86 resulting in differential peptide abundance. The sensitivity of detecting these structural changes
87 critically depends on protein sequence coverage, which can limit the analysis of low-abundance
88 proteins such as kinases in complex cell lysates[18]. While previous studies have used purified
89 recombinant proteins to address this limitation[20,21], this approach does not fully capture the native
90 context of the protein since it lacks physiological PTMs and complex partners essential for correct
91 structure and function. Therefore, we performed LiP-MS on native AP eluates (Fig. 1A). In this
92 approach, target proteins are purified from human cells under native conditions and treated with an
93 inhibitor, prior to the LiP-step with PK. Samples are then digested with trypsin and analyzed by liquid
94 chromatography coupled mass spectrometry (LC-MS).
95 We selected the serine/threonine-protein kinase DCLK1 to benchmark our approach, since X-ray crystal
96 structures are available for both the DCLK1-IN-1-bound[22,23] and unbound protein[24] (Supplementary Fig.
97 1A). AP-LiP-MS profiling of DCLK1 showed that 25 of 29 peptides with significantly altered intensity
98 were DCLK1 peptides, clearly indicating structural changes in DCLK1 upon inhibitor binding
99 (Supplementary Fig. 1B, C, 2A). This observation shows that we detect the structural changes we
100 anticipated from the X-ray structures.

101 To determine whether AID rearrangement upon inhibitor binding is a general phenomenon, we
102 investigated kinases with diverse AIDs that vary in both structure and regulatory mechanism, and for
103 which well-characterized ATP-competitive inhibitors are available. We therefore selected CAMKK2,
104 CHEK1, and PRKCA as model kinases, representing distinct modes of autoinhibition and regulatory
105 control. The AID of CAMKK2 is a small linear motif and binds the back of the KD[25]. Activation occurs
106 through binding of calmodulin to the AID, which relieves the interaction between the AID and the KD.
107 CHEK1 instead has a larger, structured AID. Its activation is triggered via phosphorylation from the
108 upstream kinase Ataxia telangiectasia and Rad3 related (ATR), which relieves the interaction between
109 the AID and the KD of CHEK1[26]. On the other hand, PRKCA has an N-terminal disordered
110 pseudosubstrate motif that dissociates from the KD upon Ca^{2+} binding[27,28]. For each of these kinases,
111 specific high-affinity ATP-competitive inhibitors have been developed: SGC-CAMKK2-1 for CAMKK2[29],
112 rabusertib for CHEK1[30], and Gö 6983 for PRKCA[31].
113 We applied AP-LiP-MS to CAMKK2, CHEK1 and PRKCA to investigate the structural consequences of
114 inhibitor binding. For all three kinases we observed a structural change at the AID upon binding of the
115 respective inhibitor (Fig. 1B-D, Supplementary Fig. 2B-G). CAMKK2 showed changes exclusively in its
116 AID. The peptide indicating the structural change at the AID is half-tryptic, meaning that one end was
117 generated by PK cleavage. The increased abundance of such peptides indicates increased PK
118 susceptibility and thus increased accessibility of the AID. This is consistent with a transition to an open
119 conformation. In addition to changes at the AID, CHEK1 and PRKCA also underwent structural
120 alterations throughout the KD. Additionally, the PRKCA inhibitor Gö 6983 led to structural changes in
121 the C2 domain, specifically at residues 260-269, which are part of a short sequence associated with
122 autoinhibition[32]. We observed increased PK accessibility of both domains, potentially reflecting an
123 allosteric disruption of the C2-KD interaction. Notably, all observed structural changes upon inhibitor
124 treatment occurred in the same regions previously described to be involved in kinase activation.
125 Specifically, the AID is known to dissociate from the KD upon activation for all investigated kinases[25,33-
126 35]. Furthermore, PRKCA activation is also associated with larger rearrangements in its membrane-
127 binding C2 domain[36]. These results suggest that kinases undergo conformational changes upon
128 inhibitor binding in regions typically associated with their activation.

129 Inhibition of CAMKK2 with SGC-CAMKK2-1 stabilizes interactions associated with 130 CAMKK2 activation

131 An open kinase conformation induced by inhibitor binding could alter the accessibility of interaction
132 surfaces hidden in the autoinhibited conformation[37]. We therefore applied AP-MS (Fig. 2A) and *in vivo*
133 proximity labeling (Fig. 2B) to profile subsequent changes in kinase complexes and proximity,
134 respectively.

135 We first measured changes in CAMKK2 complex formation. AP-MS identified 66 interactors of CAMKK2
136 across all treatments, 22 of which were previously listed in the BioGrid database[38] (Supplementary
137 Table 1). Five proteins changed in abundance in response to SGC-CAMKK2-1 (Fig. 2C, Supplementary
138 Fig. 3A, B). 5'-AMP-activated protein kinase subunit alpha-1 (PRKAA1), the catalytic subunit of the
139 trimeric AMPK complex and known substrate[39] and interactor[40] of CAMKK2, was the most strongly
140 increased protein in CAMKK2 complexes in the presence of the inhibitor. Extended synaptotagmin-2
141 (ESYT2), another known CAMKK2 interactor, was also increased but to a lesser extent than PRKAA1.
142 We also found three proteins whose interaction was reduced upon inhibitor binding. This includes a
143 strong reduction of Obscurin-like protein 1 (OBSL1), a known CAMKK2 interaction albeit of unknown
144 function and, with lower significance, the reduced abundance of metabolic enzyme ATP-dependent 6-
145 phosphofructokinase (PFKM) and the Puromycin-sensitive aminopeptidase (NPEPPS).
146 To explore changes in the interaction landscape of CAMKK2 *in vivo*, we extended our analysis by
147 proximity labeling using miniTurbo-CAMKK2 expressing cells (Fig. 2D, Supplementary Fig. 3C, D). We
148 found 71 proteins with altered proximity to CAMKK2 in the presence of the inhibitor. Gene ontology
149 (GO) enrichment analysis revealed that SGC-CAMKK2-1 caused changes in proximity to proteins related
150 to actin filament organization and metabolic processes (Fig. 2E). Among these proteins were five
151 subunits of the trimeric AMPK complex as well as known AMPK interactors, such as TP53 (Fig. 2F). The
152 increased proximity to catalytic as well as regulatory AMPK subunits suggests complex formation
153 between CAMKK2 and trimeric AMPK complexes upon SGC-CAMKK2-1 treatment. Interestingly, since
154 the CAMKK2-PRKAA1 interaction has been previously observed only in the presence of Ca^{2+}, calmodulin
155 and ATP, this interaction likely requires an active CAMKK2 conformation[41]. Thus, our observation that
156 CAMKK2 binds AMPK upon inhibition with SGC-CAMKK2-1 is consistent with the AP-LiP-MS data which
157 suggested that the inhibitor stabilizes an open, active-like kinase conformation.
158 Reassuringly, SGC-CAMKK2-1 also induced a strong increase of endogenous CAMKK2 in the proximity
159 of PRKAA1 following inhibitor treatment upon reciprocal *in vivo* proximity labeling using miniTurbo-
160 PRKAA1 expressing cells (Fig. 2G, Supplementary Fig. 3E, F), confirming our previous findings. SGC-
161 CAMKK2-1 treatment also caused a remodeling of PRKAA1 interactions beyond CAMKK2 as we
162 observed a significant enrichment for proteins linked to mitochondria and endoplasmic reticulum
163 based on a GO enrichment analysis (Fig. 2H). This suggests that CAMKK2 inhibitors may also change
164 the biochemical environment of AMPK beyond stabilizing the CAMKK2-PRKAA1 interaction.
165 Taken together, we found that SGC-CAMKK2-1 causes structural changes and remodeling of CAMKK2-
166 containing complexes, including a strong increase in CAMKK2-PRKAA1 complex formation.
167 Consequently, probe treatment extensively altered the protein environment of PRKAA1. Our data thus
168 show how an ATP-competitive kinase inhibitor can affect the interactors of both its target but also of
169 associated signaling proteins.

170 ## Sequestration of PRKAA1 by inhibitor-bound CAMKK2 inhibits PRKAA1 phosphorylation
171 by other kinases

172 The inhibitor-induced CAMKK2-AMPK complex could be caused by the observed changes in CAMKK2
173 conformation but also result from decreased AMPK phosphorylation following catalytic inhibition of
174 CAMKK2[42]. To disentangle the effects of catalytic inhibition and conformational change on the altered
175 PPIs, we compared inhibitor-induced structural changes and complex formation between wildtype
176 (WT) CAMKK2 and the following three mutants: the catalytically inactive D312A mutant[43], the R311C
177 mutant found in patients with bipolar disorder[44], and the phosphomimetic mutation T483D, which is
178 at the major autophosphorylation site of CAMKK2 associated with autonomous activity[45].
179 First, we applied AP-LiP-MS to compare structural changes between wildtype and mutant CAMKK2
180 following inhibitor treatment. We found that all tested mutants displayed a structural change at or
181 close to the AID similar to wildtype CAMKK2 in response to SGC-CAMKK2-1 (Fig. 3A, Supplementary
182 Fig. 4A-C), demonstrating that all mutants can bind the compound and respond with a conformational
183 change similar to WT CAMKK2. The structural change in the AID for the CAMKK2 T483D mutant
184 suggests that it is also in a closed conformation in the absence of the inhibitor. This is consistent with
185 previous reports showing that activity of the CAMKK2 isoform used in our study depends on calmodulin
186 binding also when autonomously active[46].
187 We subsequently analyzed CAMKK2-PRKAA1 complex formation upon SGC-CAMKK2-1 treatment
188 across the mutants (Fig. 3B, Supplementary Fig. 4D-F). Upon SGC-CAMKK2-1 treatment, both the
189 catalytically inactive D312A and the autonomously active T483D mutant displayed an interaction
190 pattern with PRKAA1 similar to wildtype CAMKK2, suggesting that these changes are not linked to
191 CAMKK2 catalytic activity but rather relate to the observed structural change. Surprisingly, the disease-
192 related CAMKK2 R311C mutation completely abolished the interaction with PRKAA1, irrespective of
193 inhibitor treatment, which could hint at a novel disease mechanism via uncoupling the CAMKK2-AMPK
194 signaling axis in patients with this genetic disorder.
195 To better understand potential implications of CAMKK2-PRKAA1 complex formation, we generated a
196 structural prediction of the two KDs using AlphaFold3[47] (Fig. 3C, Supplementary Fig. 4G, H). In the
197 predicted PPI interface of CAMKK2, we observed that R311 is oriented towards the predicted
198 interaction interface, while D312 is outside of the interaction interface (Fig. 3D). This suggests that the
199 R311C mutation may negatively affect the integrity of the interaction interface needed for PRKAA1
200 binding and may explain why the SGC-CAMKK2-1-induced interaction with PRKAA1 is abolished for
201 CAMKK2 R311C but not D312A.
202 We further investigated the predicted binding interface of PRKAA1 (Fig. 3E) and noticed that T183,
203 shown in orange, is buried in the interface of the predicted CAMKK2-PRKAA1 complex. While this
204 residue can be phosphorylated by CAMKK2 in response to increased intracellular Ca^{2+} ions, it is

205 phosphorylated upon glucose starvation primarily by liver kinase B1 (LKB1)[48]. Since PRKAA1 is bound
206 by CAMKK2 in response to SGC-CAMKK2-1, this site would become inaccessible to other upstream
207 kinases. This led us to hypothesize that formation of the CAMKK2-PRKAA1 complex would inhibit
208 PRKAA1 T183 phosphorylation by other kinases such as LKB1. We tested this hypothesis by analyzing
209 T183 phosphorylation in HEK293 cells subjected to glucose starvation and siRNA-mediated depletion
210 of CAMKK2 (Fig. 3F, Supplementary Fig. 5). We found that the glucose-induced T183 phosphorylation
211 of PRKAA1 was indeed decreased after CAMKK2 inhibition with SGC-CAMKK2-1. Importantly, this
212 decrease was rescued upon siRNA-mediated knockdown of CAMKK2, supporting a model where SGC-
213 CAMKK2-1 induced formation of CAMKK2-PRKAA1 complexes could block the T183 phosphorylation
214 and activation of PRKAA1 by other kinases.
215 We showed that inhibitor-induced changes in protein interactions cannot be simply explained by
216 inhibition of catalytic activity, and that SGC-CAMKK2-1 can regulate a non-catalytic scaffolding function
217 of CAMKK2 via conformational changes. The disease-associated mutant R311C fully inhibited CAMKK2-
218 PRKAA1 complex formation, representing first evidence for a potential molecular mechanism
219 associated with bipolar disorder linked to this mutation and emphasizing the importance of genetic
220 context for personalized drug response. Finally, we showed that SGC-CAMKK2-1 induces CAMKK2-
221 AMPK complex formation, which may represent an additional mechanism to hinder PRKAA1
222 phosphorylation by other kinases. This finding underscores the importance of exploring inhibitor-
223 induced PPI changes to broaden our understanding of multilayered target engagement mechanisms.

224 Inhibition of CHEK1 with rabusertib alters interactions with DNA-damage response 225 proteins

226 AP-LiP-MS revealed significant structural alterations in the KD and the AID of CHEK1 upon binding of
227 the inhibitor rabusertib. To understand how these changes may remodel the interactome of CHEK1,
228 we performed AP-MS and *in vivo* proximity labeling experiments. AP-MS identified 51 interactors of
229 CHEK1, of which 39 have been reported previously[38] (Supplementary Table 2). Rabusertib affected
230 CHEK1 interactions with 18 proteins (Fig. 4A, Supplementary Fig. 6A) that upon GO enrichment analysis
231 show clear enrichment for terms related to known CHEK1 functions in the DNA-damage response (Fig.
232 4B). This includes increased interaction with 14-3-3 proteins zeta (YWHAZ) and theta (YWHAQ), which
233 has also been observed upon DNA damage-induced CHEK1 activation[49]. Inhibitor treatment in addition
234 stabilized the interaction with Ubiquitin carboxyl-terminal hydrolase 7 (USP7), a deubiquitylating (DUB)
235 enzyme known to directly interact with CHEK1[50]. USP7 has increased DUB activity towards CHEK1 upon
236 DNA damage[51]. Moreover, rabusertib increased the abundance of CHEK1 complexes containing
237 proliferating cell nuclear antigen (PCNA) and the DNA replication licensing factors MCM2, MCM3,
238 MCM4, MCM5 and MCM6, which are subunits of the MCM complex. Both these interactions are
239 required for CHEK1 activation[52,53]. These proteins are part of a highly interconnected PPI network (Fig.

240 4C). The only protein we found to dissociate from CHEK1 upon rabusertib treatment was the
241 mitochondrial protein CLPB.
242 *In vivo* proximity labeling with miniTurbo-CHEK1 showed that rabusertib induced the proximity to 12
243 proteins with known functional links to CHEK1 (Fig. 4D, Supplementary Fig. 6B, C) including Aurora
244 kinase A- and ninein-interacting protein (AUNIP), transcription factor E2F8, Rap1-interacting factor 1
245 (RIF1), MCM10, the kinases tousled-like 2 (TLK2) and ATR, and the scaffolding protein DNA
246 topoisomerase 2-binding protein 1 (TOPBP1). ATR and TOPBP1 act upstream to activate CHEK1 by
247 phosphorylation on multiple sites including S317 upon DNA damage[54].
248 We therefore analyzed the abundance of phosphopeptides in purified CHEK1 complexes, and observed
249 increased phosphorylation of CHEK1 on the known ATR phosphorylation site S317 upon rabusertib
250 treatment (Fig. 4E, Supplementary Fig. 6D). This paradoxical activating phosphorylation in response to
251 CHEK1 inhibition has been noticed in the past and might be due to increased spontaneous DNA damage
252 as observed previously for other CHEK1 inhibitors[55,56] (Supplementary Fig. 6E, 7). We also observed
253 decreased CHEK1 autophosphorylation at S296 (Fig. 4E) in rabusertib-treated cells as expected upon
254 CHEK1 catalytic inhibition[57]. These phosphorylation changes might explain both the enhanced 14-3-3
255 protein binding to CHEK1, which depends on phosphorylation by ATR[49], and the increase in binding to
256 chromatin and associated proteins, as CHEK1 dissociation from these depends on S296
257 autophosphorylation[58].
258 We found that CHEK1 inhibition changes CHEK1 complex formation with many DNA-damage response
259 proteins. These changes were consistent with decreased CHEK1 activity, resulting in lower levels of
260 autophosphorylation and increased DNA damage and thus increased ATR activity towards CHEK1. We
261 show that such mechanisms can also shape the interaction landscape of an inhibited kinase.

262 CHEK1 inhibition destabilizes complexes with the mitochondrial protein CLPB and 263 causes mitochondrial fragmentation

264 Whereas the functional relevance of most of the observed interactors has been studied, the role of the
265 CHEK1-CLPB interaction change remains unknown. Several studies using different approaches have
266 identified CLPB as an interaction partner of CHEK1[9,59,60] (Fig. 5A), which strongly suggests the formation
267 of mitochondrial CHEK1 complexes of yet unknown function. We were therefore prompted to study
268 the rabusertib-induced CHEK1-CLPB dissociation in more detail. To test whether the dissociation
269 depends on the catalytic activity of CHEK1, we compared dissociation in WT CHEK1, the catalytically
270 inactive D130A mutant and the constitutively active L449R mutant, which is in an open conformation
271 that is constitutively phosphorylated by ATR[33,61]. Rabusertib treatment significantly decreased CLPB in
272 both WT and D130A CHEK1 complexes, whereas CHEK1 L449R-CLPB binding was not affected (Fig. 5B,
273 Supplementary Fig. 8A, B). This suggests that the interaction with CLPB does not depend on catalytic
274 inhibition of CHEK1.

275 Given that genetic deletion of CLPB results in mitochondrial fragmentation[62], we next analyzed
276 mitochondrial morphology in fixed HeLa cells in the presence or absence of rabusertib using super-
277 resolution microscopy (Fig. 5C). We quantified mitochondria in fragmented and elongated states and
278 identified mitochondrial areas consistent with previous analyses of human mitochondria[63,64]
279 (Supplementary Fig. 8C). Rabusertib treatment caused a significant increase in mitochondrial
280 fragmentation ($p = 4.3 \times 10^{-3}$, ANOVA followed by Tukey HSD). CHEK1 inactivation can lead to
281 premature and sustained CDK1 activation[65], which induces mitochondrial fragmentation via
282 phosphorylation of the GTPase Dynamin-1-like protein (DRP1) controlling mitochondrial fission[66,67]. To
283 exclude such a mechanism, we analyzed the mitochondrial network in response to rabusertib in
284 combination with the CDK1 inhibitor RO-3306. We confirmed the significant increase in mitochondrial
285 fragmentation even when CDK1 is inhibited by RO-3306 ($p = 1.4 \times 10^{-6}$, ANOVA followed by Tukey HSD),
286 which excludes mitochondrial fragmentation via activation of the CDK1-DRP1 axis.
287 We had noticed that CHEK1 inhibition by rabusertib can cause DNA damage similar to etoposide
288 treatment as measured by increased histone H2AX phosphorylation (Supplementary Fig. 6E, 7). We
289 therefore asked if mitochondrial fragmentation could also be detected upon etoposide-mediated DNA
290 damage. We observed a slight but non-significant increase in mitochondrial fragmentation upon
291 etoposide treatment ($p = 0.151$, two-sided t-test; Supplementary Fig. 8D). This indicates that DNA
292 damage alone cannot explain mitochondrial fragmentation by rabusertib, suggesting the involvement
293 of an additional mechanism. In this regard, rabusertib-induced dissociation of mitochondrial CHEK1-
294 CLPB complexes represents an intriguing mechanism, though further testing is needed before a causal
295 relationship can be established.
296 Taken together, we observed that CHEK1 inhibition is associated with changes in PPIs, including
297 dissociation of the known mitochondrial interactor CLPB. We showed that the interaction between
298 CHEK1 and CLPB does not depend on catalytic activity of CHEK1. Based on this finding, we investigated
299 mitochondrial phenotypes upon CHEK1 inhibition. We found that rabusertib induced a significant
300 increase in mitochondrial fragmentation upon CHEK1 inhibition by a mechanism that is independent
301 of CDK1 activation or induction of DNA damage. This illustrates how non-catalytic probe mechanisms
302 can induce novel phenotypes.

303 Inhibitor binding induces relocalization of PRKCA to cellular junctions

304 We found that upon Gö 6983 treatment, PRKCA undergoes structural rearrangements in the KD and
305 AID, but also in other domains, such as the membrane-associating C2 domain. We aimed to profile
306 related interactome changes of PRKCA using AP-MS. Following purification from native lysates
307 obtained from treated cells, we surprisingly noticed a four-fold decrease in PRKCA abundance upon Gö
308 6983 treatment (Supplementary Fig. 9A, B), limiting the sensitivity of the AP-MS approach. In contrast,
309 we observed no such decrease in PRKCA abundance in the *in vivo* proximity labeling experiment, which

310 applies harsh denaturing lysis conditions, suggesting that Gö 6983 treatment results in PRKCA
311 relocalization to a cell compartment that is insoluble under native lysis conditions.
312 To characterize the relocalization of inhibitor-bound PRKCA, we focused our analysis on *in vivo*
313 proximity labeling. This approach clearly demonstrated a Gö 6983 induced shift in PRKCA proximity
314 towards membrane associated proteins linked to cell adhesion and cellular junctions (Fig. 6A-C,
315 Supplementary Fig. 9C, D). This included the focal adhesion protein and known PRKCA interactor
316 Integrin beta-1 (ITGB1)[68], but also proteins from tight junctions (OCLN, MARVELD2, CXADR, FMN2,
317 EPB41L4B), adherens junctions (NECTIN2, SNAP23), desmosomes (DSG2) and other junction proteins
318 (ADM4, KIRREL1, MPZL1, TENM3), suggesting that PRKCA relocalizes to very specific membrane
319 structures that control cell-cell contacts and intercellular signaling upon Gö 6983 binding.
320 Under physiological conditions, the affinity of PRKCA for membrane lipids is regulated by Ca^{2+} binding[69].
321 We therefore asked if the observed relocalization to membrane structures could be explained via
322 changes in intracellular Ca^{2+} concentrations induced by Gö 6983. We however did not observe any
323 changes in cellular Ca^{2+} concentration upon Gö 6983 treatment using a Fluo-4 calcium imaging assay
324 (Supplementary Fig. 9E). We therefore excluded the possibility that Gö 6983 alters the biochemical
325 context of PRKCA via changes in Ca^{2+} concentration, and proposed a model where Gö 6983 binding to
326 PRKCA directly affects the affinity of the kinase for membranes or membrane proteins.
327 To explore whether catalytic activity is needed for the observed proximity changes, we compared Gö
328 6983-induced proximity patterns between WT PRKCA, the catalytically inactive PRKCA D463A mutant
329 and the constitutively active R22A/A25E double mutant[70]. When inhibited, we found similar changes
330 in the proximity of PRKCA WT and both mutants towards the cellular junction proteins (Fig. 6D, cluster
331 1, Supplementary Fig. 9F, G), suggesting that these changes are independent of catalytic inhibition.
332 Other proximity changes were affected in the mutants compared to the WT (Fig. 6D, cluster 2 and 3),
333 suggesting that these changes may depend on the catalytic activity or the conformation of the AID.
334 We next compared our biochemical findings to subcellular localization patterns using live-cell imaging
335 of cells expressing EGFP-PRKCA. Indeed, consistent with our proximity data, we observed Gö 6983-
336 induced relocalization of PRKCA towards the cell periphery, especially at cell-cell contact sites, within
337 8 minutes (Fig. 6E). In addition to the increased interaction with the plasma membrane, we also noticed
338 localization towards unknown cytoplasmic foci. Since we saw no enrichment for proteins associated
339 with intracellular organelles, these foci might represent PRKCA aggregates or endosomes containing
340 cell-junction proteins[71].
341 In summary, we observed that Gö 6983 caused a rapid relocalization of PRKCA towards the plasma
342 membrane, specifically towards complexes involved in cell adhesion and cellular junctions. These
343 changes were observed also in the catalytically inactive and constitutively active mutants upon Gö
344 6983 treatment, suggesting that these changes are not related to the inhibition of PRKCA kinase

activity. PRKCA is known to associate with the plasma membrane through direct contact with lipids upon activation via its C2 domain[72]. Since our AP-LiP-MS data suggest that Gö 6983 binding can trigger structural changes in the C2 domain, we propose that these structural changes expose the C2 domain for subsequent recruitment of PRKCA to specific membrane structures.

Discussion

ATP competitive kinase inhibitors are primarily designed to block the catalytic activity of their target, but their effect on kinase conformation and non-catalytic functions remains poorly explored. X-ray crystallography studies revealed that type I and II inhibitors can stabilize either an active DFG-in or inactive DFG-out conformation of the KD, respectively[73]. The DFG-in and DFG-out classification, although initially useful, turned out to be insufficient to fully explain drug action and cellular phenotypes. Our study suggests that the ATP-binding site is a major organizing center of kinase conformation and interaction, regulating contacts with AIDs, other regulatory domains and even other proteins. ATP-competitive inhibition disrupts these domain-domain interactions, resulting in active-like kinase configurations that drive molecular events including regulation of non-catalytic functions like complex formation or relocalization.

Using AP-LiP-MS, we detected structural changes distal from the orthosteric binding sites for all kinases analyzed, suggesting that inhibitor-induced allostery is a more pervasive feature of type I inhibitor binding. These changes are best explained by dissociation of the AID from the KD, a mechanism that mimics the conformational unlocking observed during physiological kinase activation. The observation that the AID is more solvent-exposed upon inhibitor binding and thus in the open conformation, together with previous reports that these inhibitors stabilize the active, DFG-in conformation of the KD[29,74,75], indicates that the inhibitor-bound conformations closely resemble the active kinase structure. This is corroborated by our finding that the probe-bound conformation facilitates the formation of kinase complexes typically found only upon activation of CAMKK2, CHEK1 and PRKCA.

Contextual proteomics revealed important new insights into neomorphic drug effects for all three models tested. In our first model, the CAMKK2 inhibitor SGC-CAMKK2-1, besides blocking CAMKK2 kinase activity, induced stable complex formation with PRKAA1. Our data and structural modeling suggest that SGC-CAMKK2-1 locks CAMKK2 in a conformation that sequesters PRKAA1, shielding its Thr183 from phosphorylation by upstream kinases like LKB1. Therefore, SGC-CAMKK2-1 binding may result in a pan-AMPK inhibition which shuts down both the calcium branch (via direct catalytic inhibition) and the energy stress arm (via sequestration). Such a dual AMPK inhibitor role may offer novel means to modulate AMPK-dependent energy signaling in tissues expressing CAMKK2 such as the central nervous system.

In our second model, CHEK1 inhibitor rabusertib disrupted CHEK1 complex formation with CLPB, a known CHEK1 interactor controlling mitochondrial homeostasis and stress responses[9,59,60]. While the

380 precise function of this CHEK1-CLPB interaction remains to be fully resolved, it may regulate
381 mitochondrial integrity. CLPB is known to maintain the solubility of the anti-apoptotic regulator
382 HAX1[76]—which interacts with both CHEK1[9,60,77] and CLPB[59,77,78]—allowing HAX1 to inhibit Caspase-9[79].
383 Furthermore, loss of CLPB has been linked to mitochondrial fragmentation[62]. Strikingly, we observed
384 that rabusertib disrupts the CHEK1-CLPB interaction and causes mitochondrial fragmentation, even
385 when CDK1 is inhibited. This finding rules out the canonical mechanism where CHEK1 inhibition drives
386 fragmentation via promoting CDK1-mediated DRP1 activation[66,67]. Instead it suggests a mechanism
387 independent of CHEK1 catalytic activity, potentially involving OPA1, an established client of CLPB[78]. In
388 the absence of CLPB, OPA1 aggregates and levels are greatly reduced resulting in mitochondrial
389 fragmentation[80]. While a direct functional link remains to be characterized, these findings suggest that
390 CHEK1 may act as a regulator for the CLPB-mediated proteostasis machinery, effectively coupling the
391 DNA damage response to the maintenance of mitochondrial structural integrity.
392 Finally, the PRKCA example illustrates how inhibitor-modulated domain-domain interactions can
393 redirect PRKCA to specific subcellular compartments. As with the other kinases, we detected structural
394 changes in the AID of PRKCA. Additionally, we also identified structural changes in a segment required
395 for PRKCA autoinhibition within the C2 domain[32], suggesting that multiple autoinhibitory domain-
396 domain interactions are disrupted by Gö 6983 binding. The C2 domain is also required for membrane
397 recruitment following PRKCA activation[69,81]. Consistent with these structural alterations, contextual
398 proteomics indeed showed that inhibitor binding strongly induced the proximity of PRKCA to specific
399 membrane proteins at cellular junctions, a phenotype we validated using live-cell imaging. Membrane
400 recruitment under physiological conditions occurs upon PRKCA activation in response to Ca^{2+} and
401 requires both the C1 and the C2 domain. Whereas C1 domain binds DAG[82], it has been proposed that
402 the C2 domain can bind phosphatidylserine (PS) upon Ca^{2+} signaling and phosphatidylinositol 4,5-
403 bisphosphate (PIP2) via a lysine cluster[83,84]. Given that PIP2 is concentrated at the apical surface and
404 tight junctions[85] it is plausible that PRKCA recruitment to cell junction complexes may result from
405 inhibitor induced opening of the C2 domain, which exposes the C2 lysine cluster for subsequent PIP2
406 binding at cellular junctions. Besides PIP2 tethering, it is also possible that PRKCA may be stabilized at
407 the membrane via direct PPIs, for example via binding ITGB1[68]. Although the downstream effects of
408 relocalizing inhibited PRKCA to cellular junctions are not yet fully understood, this potential for
409 disrupting junctional architecture and intercellular signaling necessitates a broader evaluation of
410 PRKCA inhibitors beyond their primary catalytic targets before their clinical application.
411 All three examples illustrate the breadth of catalysis-independent effects that can be induced upon
412 type I inhibitor binding. They also suggest that inhibitor-induced non-catalytic gain-of-function is a
413 more frequent phenomenon than currently anticipated. The majority of the 94 FDA approved kinase
414 inhibitors are type I inhibitors[86], yet we have reliable information on non-catalytic effects for only a

415 few of these drugs. For instance, the FDA approved JAK2 inhibitor ruxolitinib prevents the interaction
416 with tyrosine phosphatases by altering the conformation of the KD resulting in paradoxical
417 hyperphosphorylated JAK2[87]. This primes JAK2 and causes a sudden increase in JAK2 activity after
418 inhibitor dissociation, explaining major side effects in patients after drug withdrawal[88]. Another
419 prominent example is the type I BRAF inhibitor GDC-0879, which paradoxically causes activation of
420 downstream mitogen-activated protein kinase (MAPK) signaling and cell proliferation via an allosteric
421 mechanism promoting dimerization between BRAF and CRAF[89,90] even though the inhibitor was
422 designed to inhibit this pathway. These paradoxical inhibitor responses were largely discovered
423 serendipitously at late stages or post-approval.
424 The limited number of currently reported allosteric inhibitor responses reflects the limitations and
425 inherently low throughput of traditional structural methods. Previous analyses often used highly
426 purified, and usually truncated, recombinant proteins which lack key interaction partners, PTMs and
427 domains. Multimodal proteomic target engagement analysis as presented here represents an
428 important step to overcome previous limitations by enabling high throughput detection and
429 characterization of allosteric inhibitor effects across the kinase family and beyond. Systematic
430 characterization of such mechanisms during early drug development could help to reduce the high
431 failure rate and could guide the development of safer and more effective therapeutics.
432 We therefore advocate for the systematic multiproteomic characterization of such off-mechanism
433 effects during inhibitor development. Recent advances in LC-MS instrumentation now provides the
434 scalability needed for systematic target engagement profiling[91]. Crucially, the combination of structural
435 and contextual proteomics is not restricted to kinases and can be applied to a broad range of targets
436 to develop new classes of inhibitors targeting also proteins with no known catalytic activity. By
437 systematically mapping inhibitor modulated conformational and interactome landscapes, we can
438 better understand drug phenotypes and reduce the failure rate of future therapeutics by detecting
439 neomorphic liabilities early during drug development.

440 Methods

441 Generation of expression constructs

442 We generated doxycycline-inducible expression vectors of N-terminal Strep-HA-tagged, miniTurbo-
443 tagged or EGFP-tagged bait proteins using the destination vectors pcDNA5-FRT-TO-SH-GW[92], pcDNA5-
444 pDEST-FRT-MiniTurbo-Flag-N-term, or pcDNA5-pDEST-FRT-EGFP-Flag-N-term, respectively. Human
445 ORFs were provided as pDONR223 vectors selected from addgene, Gateway compatible human
446 orfeome collections horfeome v5.1, horfeome v8.1 and ORFeome Collaboration Clones[93]
447 (OpenBiosystems, Horizon Discovery) or from a kinome orf collection[94] (Supplementary Table 3).
448 Mutations were introduced using a QuickChange II Site-Directed Mutagenesis Kit (Agilent) with primers
449 listed in Supplementary Table 4. The LR reaction was done as described previously[95]. In brief, 150 ng

450 of the destination vector and 300ng of the pDONR223 vector were mixed and diluted with TE buffer
451 (pH 8.0) to a total volume of 4 µL. LR reaction was performed with 1 µL of LR Clonase II enzyme mix
452 (Thermo Fisher Scientific) at 25°C for 1 h and transformed into OmniMAX competent *E. coli* cells
453 (Thermo Fisher Scientific). The transformation mixture was plated onto LB plates containing 100 µg/ml
454 ampicillin and incubated at 37°C o/n and plasmid DNA was isolated from individual colonies by using a
455 QIAprep Spin Miniprep kit (Qiagen) according to the manufacturer's instructions and confirmed by
456 sequencing.

457 Generation of stable inducible cell lines

458 The stable inducible cell lines were generated as described previously[95] with the following alterations:
459 3 x 10^5 T-Rex-HEK293 Flp-In cells (R78007, Invitrogen) were seeded onto six-well plates in DMEM
460 supplemented with 10% fetal bovine serum (FBS) and 1% penicillin-streptomycin (P/S) and incubated
461 at 37°C and 5% CO_2 o/n. The cells were transfected with the following mixture: 100 ng of the respective
462 expression vector, 900 ng of pOG44 (Invitrogen), 5.7 µl x-tremeGENE 9 DNA transfection reagent
463 (Roche) and 94.3 µl DMEM. The mixture was incubated for 15 minutes at room temperature and added
464 to the cells. The next day, new DMEM supplemented with 10% fetal bovine serum (FBS) and 1%
465 penicillin-streptomycin (P/S) was added. The following day the cells were split into a T150 flask with a
466 total volume of 32 ml. The next day hygromycin B was added at a final concentration of 100 µg/ml and
467 hygromycin resistant recombinant cell pools were selected. Each new cell line was mycoplasma tested
468 before use in experiments.

469 Cultivation of cells for AP-LiP-MS and AP-MS experiments

470 HEK293 cells inducibly expressing the strep-HA-tagged bait proteins or EGFP (for AP-MS only) were
471 seeded at a density of 10^7 in 25 ml DMEM supplemented with 10% FCS (BioConcept) and 1% P/S in a
472 15 cm dish. The cells were incubated at 37°C and 5% CO_2 o/n. Protein expression was induced with 1.3
473 µg/ml doxycycline for 24 hours before treatment with 1 µM inhibitor (SGC-CAMKK2-1: Sigma;
474 rabusertib: Med Chem Express; Gö 6983: Med Chem Express) or 0.01% DMSO for 4 hours. Per sample,
475 cells from two 15 cm dishes were harvested by scraping in cold PBS. Each sample was washed in PBS
476 and flash frozen in liquid nitrogen.

477 Cultivation of cells for proximity labeling experiments

478 HEK293 cells inducibly expressing the miniTurbo-tagged bait proteins or EGFP were seeded at a density
479 of 10^7 in 25 ml DMEM supplemented with 10% dialyzed FCS (BioConcept) and 1% P/S in a 15 cm dish.
480 The cells were incubated at 37°C and 5% CO_2 o/n. Protein expression was induced with 1.3 µg/ml
481 doxycycline for 24 hours before they were treated with 1 µM inhibitor or 0.01% DMSO for 4 hours. An
482 hour before harvesting, cells were treated with 50 µM biotin. Cells were harvested by dissociation in
483 cold PBS with 1 mM EDTA. Each sample was washed in PBS and flash frozen in liquid nitrogen.

484 ## AP-LiP-MS

485 Pellets were lysed by resolubilizing in 2 ml HNN buffer (50 mM HEPES pH 8.0, 150 mM NaCl, 50 mM
486 NaF) supplemented with 0.5% IGEPAL, 400 nM Na_3VO_4, 1 mM PMSF and 0.2% Protease Inhibitor
487 Cocktail (Sigma). The lysate was incubated on ice for 10 minutes and centrifuged at 18000x g for 20
488 minutes at 4˚C. The supernatant was added to 80 µl StrepTactin Sepharose slurry (IBA Lifesciences)
489 and incubated on a rotating wheel for 60 minutes at 4˚C. The beads were loaded onto a 1 µm glass
490 filter column and washed 3 times with 1 ml HNN buffer supplemented with 0.5% IGEPAL and 400 nM
491 Na_3VO_4, 3 times with 1 ml HNN buffer, and 3 times with LiP buffer (1 mM $MgCl_2$, 150 mM KCl and 100
492 mM HEPES pH 7.5). Samples were eluted twice by incubation with 30 µl of 0.5 mM biotin in LiP buffer
493 for 15 minutes. The eluate was pooled and the total protein concentration was determined using a
494 BCA protein assay kit (Pierce) according to the manufacturer's protocol. Measured protein
495 concentrations were between 0.06 µg/µl and 0.1 µg/µl. For each sample, 50 µl eluate was used.
496 Samples were then processed as previously described[96]. Briefly, samples were treated with 10 µM
497 inhibitor or 2% DMSO in triplicates and incubated at 25˚C for 5 minutes. Proteinase K (Sigma) at an
498 enzyme:substrate ratio of 1:100 was added for 5 minutes. Proteolysis was stopped by incubation at
499 99˚C for 5 minutes. Samples were then diluted with 10% sodium deoxycholate (DOC) for a final
500 concentration of 5% DOC. Samples were reduced with 5 mM TCEP for 40 minutes at 37°C and 200 rpm,
501 and alkylated with 40 mM IAA for 30 minutes at 30°C in the dark, at 200 rpm. Samples were diluted
502 with 100 mM ammonium bicarbonate to a DOC concentration of 1%. To each sample, 1 µg Lys-C and
503 1 µg trypsin was added and samples were incubated o/n at 37°C and 200 rpm. The digestion was
504 stopped with 2% formic acid (FA) and precipitated DOC was removed by filtration using 0.2 µm PVDF
505 filters.

506 ## AP-MS

507 Cell pellets were lysed by resolubilizing in 2 ml HNN buffer supplemented with 0.5% IGEPAL or 1% DDM
508 when using PRKCA as bait, 400 nM Na_3VO_4, 1 mM PMSF, 0.2% Protease Inhibitor Cocktail (Sigma) and
509 0.5 µl/ml benzonase (Sigma). The lysate was incubated on ice for 10 minutes and centrifuged at 18000x
510 g for 20 minutes at 4˚C. The pulldown was done as for AP-LiP-MS samples, except that the final wash
511 was done with 100 mM ammonium bicarbonate. Samples were eluted twice by incubation with 30 µl
512 of 0.5 mM biotin in 100 mM ammonium bicarbonate for 15 minutes. To the samples, 60 µl 8 M urea in
513 100 mM ammonium bicarbonate for a final concentration of 4 M urea. Samples were reduced and
514 alkylated as for AP-LiP-MS. Samples were diluted with 100 mM ammonium bicarbonate to a urea
515 concentration of 1 M. To each sample, 1 µg Lys-C and 1 µg trypsin was added and samples were
516 incubated o/n at 37°C and 200 rpm. The digestion was stopped with 2% FA.

517 ## *In vivo* proximity labeling

518 Cell pellets were lysed in 1 ml RIPA buffer (50 mM Tris-HCl pH 8, 150 mM NaCl, 1 % Triton, 1mM EDTA,
519 0.1 % SDS) supplemented with 1 mM PMSF, 0.2% Protease Inhibitor Cocktail (Sigma) and 0.5 µl/ml
520 benzonase (Sigma). The lysate was briefly sonicated for 30 s, incubated at 10˚C for 30 minutes and
521 centrifuged at 18000x g for 20 minutes at 4˚C. The supernatant was added to protease resistant 120 µl
522 StrepTactin Sepharose slurry (IBA Lifesciences) that were modified as previously described[97] and
523 incubated on a rotating wheel for 60 minutes at 4˚C. The beads were loaded onto a 1 µm glass filter
524 plate and washed 3 times with 1 ml RIPA buffer, 3 times with 1 ml HNN buffer, 3 times with 100 mM
525 ammonium bicarbonate and transferred to a 10 kDa cutoff plate and centrifuged at 1500x g for 15
526 minutes. To the samples, 100 µl of 8 M urea was added. Samples were reduced with 10 mM TCEP for
527 30 minutes at 37 °C and 200 rpm, and alkylated with 40 mM IAA for 30 minutes at 37°C in the dark, at
528 200 rpm. Following centrifugation at 1500x g for 15 minutes, beads were washed twice with 250 µl of
529 100 mM ammonium bicarbonate and resuspended in 200 µl of 100 mM ammonium bicarbonate.
530 Samples were digested o/n at 37°C at 200 rpm in the presence of 1 µg trypsin and 1 µg Lys-C. Peptides
531 were collected by centrifugation at 1500x g for 20 minutes from the supernatant and combined with
532 the peptides from the supernatant obtained from washing the digested beads with 100 µl of 100 mM
533 ammonium bicarbonate and centrifugation at 1500x g for 40 minutes. The digestion was stopped with
534 5% FA.

535 ## Desalting

536 Samples were desalted using HNFR S18V desalting plates (Nest Group). The resin was activated using
537 200 µl methanol and washed 3 times with 200 µl Buffer B (50% ACN and 0.1% FA for AP-LiP and AP
538 samples, 40% ACN and 0.1% FA for proximity labeling samples). The resin was equilibrated 3 times with
539 200 µl Buffer A (0.1% FA for AP-LiP and AP samples, 5% ACN and 0.1% FA for proximity labeling
540 samples). Samples were loaded and washed 3 times with 200 µl Buffer A. Samples were eluted twice
541 with 100 µl Buffer B and dried in a vacuum centrifuge.

542 ## Mass spectrometry

543 AP-LiP-MS, AP-MS and PRKCA proximity labeling experiments were measured on a Orbitrap Fusion
544 Lumos Tribrid mass spectrometer (Thermo Fisher Scientific) equipped with an Acquity M-Class UPLC
545 System (Waters). To separate the peptides on self-pack 40 cm x 0.75 µm fritted emitter (CoAnn) packed
546 with 3 µm C18 beads (Dr. Maisch), we used a linear gradient of 3% to 35% acetonitrile in water with
547 0.1% FA over the course of 120 minutes at flow rate of 300 nl/min. Library samples consisting of pools
548 of replicates were measured by DDA. The MS1 spectra were acquired in a scan range of 350-1150m/z
549 with an Orbitrap resolution of 120000. The normalized automatic gain control (AGC) target was set to
550 200% with a maximum injection time of 100 ms. The RF lens was set to 30%. The targeted MS2 spectra
551 were acquired for the top 20 peaks in the spectrum and fragmented with a HCD of 30%. The spectra

552 were measured with an Orbitrap resolution of 30000 with isolation windows of 1.6 m/z. The AGC target
553 was set to 200% with a maximum injection time of 54 ms. Samples for quantification were measured
554 by DIA. The MS1 spectra were acquired in a scan range of 350-1400 m/z with an Orbitrap resolution of
555 120000. The normalized AGC target was set to 50% with a maximum injection time of 100 ms. The RF
556 lens was set to 30%. The targeted MS2 spectra were acquired for the desired masses with variable
557 isolation windows (Supplementary Table 5) and fragmented with a HCD of 28%. The spectra were
558 measured with an Orbitrap resolution of 30000 with variable scan ranges. The AGC target was set to
559 200% with a maximum injection time of 54 ms. The RF lens was set to 30%.
560 Proximity labeling samples were measured on an Orbitrap Exploris 480 mass spectrometer (Thermo
561 Fischer Scientific) equipped with an EASY-nLC 1000 System (Thermo Fischer Scientific). Peptides were
562 separated on the same column used for the Orbitrap Fusion Lumos Tribrid mass spectrometer using a
563 linear gradient of 5% to 30% acetonitrile in water (0.1% FA) over the course of 120 minutes at flow rate
564 of 300 nl/min. Library samples consisting of pools of replicates were measured by DDA. The MS spectra
565 were acquired at an Orbitrap resolution of 120000 between 350 m/z and 1500 m/z. The normalized
566 AGC target was set to 200% or a maximum injection time of 100 ms. Subsequently, 20 MS/MS spectra
567 were acquired after higher-energy collisional dissociation (HCD) with a normalized collision energy of
568 30%, an Orbitrap resolution of 30000, and a normalized AGC target of 200% or a maximum injection
569 time of 54 ms. Precursors with a minimum intensity of 5000 ion counts and a charge state between 2
570 and 6 were selected with a mass window of 1.4 m/z. A dynamic exclusion window of 20 s was used.
571 Samples for quantification were measured by DIA. The MS1 spectra were acquired in a scan range of
572 350-1150m/z with an Orbitrap resolution of 120000. The normalized AGC target was set to 200% with
573 a maximum injection time of 264 ms. The RF lens was set to 50%. The targeted MS2 spectra were
574 acquired for the desired masses with variable isolation windows (Supplementary Table 6) and
575 fragmented with a HCD of 30%. The spectra are measured with an Orbitrap resolution of 30000 with
576 variable scan ranges. The AGC target was set to 200% with a maximum injection time of 66 ms. The RF
577 lens was set to 50%.

578 ## Search of Mass Spectrometry data

579 Spectra were searched using Spectronaut v. 19 in directDIA mode with the measured DDA library files
580 used to extend the library. Searches were done separately for each experiment and bait. For AP-LiP-
581 MS and AP-MS data, semi-specific peptides were included in the search, and phosphorylation was
582 included as a variable modification. For proximity labeling data, only specific peptides were included
583 in the search, and the number of missed cleavages allowed was four. Both biotinylation and
584 phosphorylation were included as variable modifications. For all searches, cross-run normalization was
585 turned off. Report files were exported and imported into R version 4 and analyzed using protti version
586 0.6.0[98].

587 ## Determination of structural changes in AP-LiP-MS data

588 The code for all analyses is available on github.com/vivreb/multi-proteomic_profiling_of_kinases/.
589 Identified peaks were filtered for q-value < 0.001, $\log_2$(intensity) > 10 and Δrt < 0.1 minutes, where Δrt
590 was defined as the difference between the predicted retention time and the empirical apex retention
591 time. Peptides were filtered for proteotypicity and common contaminants were removed. Only
592 peptides that were complete across all conditions were used for further analysis. Peptide abundance
593 was normalized based on rank invariant values using the MBQN package[99]. Differential abundance was
594 calculated using a moderated t-test[100]. Multiple testing correction was performed using the Benjamini-
595 Hochberg procedure[101]. Peptides with an absolute $\log_2$(fold change) > 0.585 (corresponding to a fold
596 change > 1.5) and adjusted p-value < 0.05 were considered significantly changing.

597 ## Determination of interactors in AP-MS data

598 Identified peaks were filtered for q-value < 0.001, $\log_2$(intensity) > 9 and Δrt < 1 minute. Peptides were
599 filtered for specificity and proteotypicity. Only peptides that were found in all replicates within a given
600 condition were used for further analysis. Peptide abundance was normalized based on rank invariant
601 values using the MBQN package[99] and bait normalized. Protein abundance was calculated by
602 MaxLFQ[102] for proteins with at least 3 peptides. We used a modified version of the weighted D-score[103]
603 to determine interactors. First, we used protein intensity instead of spectral count, and we augmented
604 the D-score 1.1-fold for known interactors based on physical interactions in the BioGrid database[38].
605 We consider proteins that have a modified D-score > 1.425 as interactors (Supplementary Fig. 10A).
606 We confirmed that we effectively recover known interactors using a ROC area under the curve (AUC)
607 analysis (AUC = 0.992, Supplementary Fig. 10B).

608 ## Determination of interaction changes in AP-MS data

609 Peptides were filtered and normalized as for the determination of interactors before imputation using
610 msImpute[104] and protein abundance calculation using MaxLFQ[102]. For all interactors, the differential
611 abundance was calculated using a moderated t-test[100]. Multiple testing correction was performed
612 using the Benjamini-Hochberg procedure[101]. Proteins with an absolute $\log_2$(fold change) > 1 and
613 adjusted p-value < 0.05 were considered significantly changing.

614 ## Determination of phosphorylation changes in AP-MS data

615 Filtering was done as for the AP-LiP-MS analysis. Peptide abundance was normalized based on rank
616 invariant values using the MBQN package[99] and bait normalized. Only peptides complete in at least
617 one condition were kept for further analysis, and peptides were imputed using msImpute[104]. Only
618 peptides containing a phosphorylation were considered for the analysis. Differential abundance was
619 calculated using a moderated t-test[100]. Multiple testing correction was performed using the Benjamini-

620 Hochberg procedure[101]. Peptides with an absolute $\log_2$(fold change) > 0.585 (corresponding to a fold
621 change > 1.5) and adjusted p-value < 0.05 were considered significantly changing.

622 Determination of proximity changes in proximity labeling data

623 Identified peaks were filtered for q-value < 0.0001, $\log_2$(intensity) > 9 and Δrt < 0.5 minutes. Peptides
624 were filtered for proteotypicity and common contaminants were removed. Peptide abundance was
625 normalized based on rank invariant values using the MBQN package[99]. Protein abundance was
626 calculated by MaxLFQ[102] for proteins with at least 3 peptides. Differential abundance was calculated
627 using a moderated t-test[100]. Multiple testing correction was performed using the Benjamini-Hochberg
628 procedure[101]. The same calculations were performed for an EGFP control, and proteins showing a
629 change in the same direction as in the control were removed from the data. Adjusted p-values were
630 recalculated for the revised dataset. Proteins with an absolute $\log_2$(fold change) > 1 and adjusted p-
631 value < 0.05 were considered significantly changing.

632 siRNA-mediated knockdown

633 HEK293 cells (ATCC) were seeded at 10^5 cells per well in a 6-well plate in DMEM supplemented with
634 10% dialyzed FBS (BioConcept). To each well, 50 µM siRNA (siCAMKK2: s20926, Thermo Fisher
635 Scientific; siNEG: iSilencer/i Negative Control No. 1, Thermo Fisher Scientific) and 7 µl siPORT NeoFX
636 transfection reagent (Thermo Fisher Scientific) was added. Cells were grown for 72 h. Samples were
637 treated with 10 µM SGC-CAMKK2-1 for 4 h in 0.01% DMSO and glucose starved for 20 min in glucose-
638 free DMEM (Gibco) supplemented with 10% dialyzed FBS (BioConcept) before harvesting. Samples
639 were harvested in 100 µl RIPA buffer supplemented with PI, PMSF, Na3VO4 and 0.5µg/ml benzonase
640 and snap frozen. Samples were stored at -80˚C until processing.

641 Western blot analysis

642 Samples were thawed on ice, and centrifuged at 18000x g for 20 minutes and the supernatant was
643 collected. Total protein concentration was measured using a BCA assay (Pierce), and the samples were
644 diluted to 2.5 µg/µl. The samples were mixed with 4x Lämmli buffer (Invitrogen) and heated to 95°C
645 for 5 minutes. Of the samples, 20 µl were loaded onto pre-cast 4-12% Bis-Tris gels (Invitrogen) along
646 with 5 µl of the ladder (BioRad). The gel was run at 100 V for 60 minutes. The gel was blotted onto a
647 nitrocellulose membrane (BioRad) for 30 minutes. The membrane was blocked with 5% milk in TBST
648 (20 mM Tris pH 7.6, 150 mM NaCl, 1% TWEEN 20) for 1 h. The primary antibody (anti-pT183 PRKAA1:
649 Cell Signaling Technology (D4D6D); anti-PRKAA1: Cell Signaling Technology (2532); anti-CAMKK2:
650 Proteintech (11549-1-AP); anti-γH2AX: Merck (05-636); anti-H2AX: Sigma (PLA0023); anti-GAPDH:
651 Invitrogen (GA1R)) was added for 2 h at room temperature or o/n at 4˚C and subsequently washed for
652 3x 10 minutes with TBST. The secondary antibody (anti-mouse secondary antibody: Cell Signaling
653 Technology (7076S), anti-rabbit secondary antibody: Cell Signaling Technology (7074S); all diluted

654 1:1000) was added for 1 hour at RT. The membrane was again washed for 3x 10 minutes. The ECL
655 detection reagent (Cytiva) was added and the membrane was imaged by chemiluminescence with
656 various exposure times. The antibodies were removed by incubation in western blot stripping buffer
657 (Invitrogen) for 10 min, washed in TBST and blocked before the next antibody was added.

658 AlphaFold3 Prediction and Structural Analysis

659 The AlphaFold3[47] prediction of the CAMKK2-PRKAA1 complex was generated using the AlphaFold3
660 webserver (alphafoldserver.com/). Only the sequences of the KDs were used (Supplementary Table 7).
661 The interface analysis was done in the PyMOL Molecular Graphics System version 2.5.3. The interface
662 comprises residues that are within 2.8 Å of the other protein and show a change in accessible surface
663 area (ΔASA) of at least 1 $Å^2$ upon binding the interaction partner.

664 Live cell imaging

665 HEK293 cells expressing N-terminally tagged EGFP-PRKCA were seeded at 10^5 cells in 35 mm glass-
666 bottom cell culture dishes (Ibidi) in DMEM supplemented with 10% dialyzed FBS (BioConcept) and 1%
667 P/S, and induced for 24 h with 1.3 µg/ml doxycycline. For imaging, FluoroBrite DMEM (Gibco)
668 supplemented with 10% dialyzed FBS (BioConcept), 1% P/S and 1.3 µg/ml doxycycline was used. To the
669 cells, 1 µM Gö 6983 in 0.01% DMSO diluted in 100 µl imaging medium was added and cells were
670 immediately imaged using an instant Structured Illumination Microscope (VisiTech). Z-stacks were
671 acquired across 5 time points 2 minutes apart. Images were deconvolved using Huygens Professional
672 24.10. Individual slices from representative cells were normalized and cropped using ImageJ and a scale
673 bar showing 5 µm was added.

674 Immunofluorescence microscopy

675 HeLa CCL2 cells (ATCC) were seeded at 10^5 cells per well in a 6-well plate containing cover slips in
676 DMEM supplemented with 10% dialyzed FBS (BioConcept) and 1% P/S and grown o/n. To the cells, 1
677 µM rabusertib for 4 h, 6 µM RO-3306 (Sigma) for 24 h, or 50 µM etoposide (Sigma) for 3 h was added
678 in 0.01% DMSO. The cells were incubated with 100 nM MitoTracker Deep Red FM (Invitrogen) for 1 h.
679 Cells were subsequently washed with warm PBS and fixed with 4% PFA in PBS (Invitrogen) for 15
680 minutes. Cells were washed and the coverslips mounted on slides using ProLong Diamond mounting
681 medium (Invitrogen). Z-stacks of the samples were imaged using an instant Structured Illumination
682 Microscope (VisiTech). Images were deconvolved using Huygens Professional 24.10 and cropped using
683 ImageJ. Image segmentation was performed in Ilastik 1[105]. The number of pixels from fragmented
684 mitochondria were counted and normalized based on the total number of pixels from mitochondria in
685 each image. Significance was calculated per experiment. To assess significance of rabusertib treatment
686 with and without RO-3306 treatment, we used two-way analysis of variance (ANOVA) followed by a

687 Tukey Honestly Significant Difference (HSD) test. To separately test the effects of etoposide treatment,
688 we used a two-tailed t-test. 10 images taken from 3 replicates were quantified for each condition.

689 Fluo-4 calcium imaging

690 HEK293 cells ectopically expressing miniTurbo-PRKCA were grown in DMEM supplemented with 10%
691 dialyzed FBS (BioConcept) and 1% P/S, induced with 1.3 µg/ml doxycycline and treated with 1 µM Gö
692 6983 or 0.01% DMSO for 4 h. Fluo-4 solution was prepared according to manufacturer's instructions
693 (Invitrogen). Baseline fluorescence was measured with an excitation wavelength of 483 nM and an
694 emission wavelength of 530 nM every 58 seconds for 10 cycles. To the samples, 10 µM ionomycin or
695 1% ethanol, or 1 µM Gö 6983 or 1% DMSO was added. After addition of the reagents, the
696 measurements were repeated for 250 additional cycles. Measurements were normalized to a baseline
697 control without the Fluo-4 reagent and to the respective vehicle control. All measurements were done
698 in six replicates and mean and standard error of the mean were reported.

699 Data and code availability

700 All MS data and related files are accessible via the ProteomeXchange Consortium[106] via the PRIDE
701 partner repository with the dataset identifier PXD069830. All code and additional data necessary to
702 fully reproduce all analyses is available for download on github via github.com/vivreb/multi-
703 proteomic_profiling_of_kinases/.

704 Disclosure and competing interest statement

705 P.P. is an inventor on a patent that covers the LiP-MS method, a component of the pipeline presented
706 in this manuscript. The remaining authors declare no competing interests.

707 Acknowledgements

708 We thank the group of Dr. Anne-Claude Gingras for the pcDNA5-pDEST-FRT-MiniTurbo-Flag vectors.
709 We thank Dr. Natalie de Souza for her comments on the manuscript. We thank ScopeM for their
710 support and assistance with microscopy experiments. This work was supported by the Innovative
711 Health Initiative 2 Joint Undertaking (JU) under grant agreement No 875510. The JU receives support
712 from the European Union's Horizon 2020 research and innovation program and EFPIA and Ontario
713 Institute for Cancer Research, Royal Institution for the Advancement of Learning McGill University,
714 Kungliga Tekniska Hoegskolan, Diamond Light Source Limited.

715 References

716 1. Manning, G., Whyte, D.B., Martinez, R., Hunter, T., and Sudarsanam, S. (2002). The protein
717 kinase complement of the human genome. Science 298, 1912-1934.
718 https://doi.org/10.1126/science.1075762.

719 2. Lahiry, P., Torkamani, A., Schork, N.J., and Hegele, R.A. (2010). Kinase mutations in human
720 disease: interpreting genotype-phenotype relationships. Nat Rev Genet 11, 60-74.
721 https://doi.org/10.1038/nrg2707.
722 3. Torkamani, A., Verkhivker, G., and Schork, N.J. (2009). Cancer driver mutations in protein
723 kinase genes. Cancer Lett 281, 117-127. https://doi.org/10.1016/j.canlet.2008.11.008.
724 4. Drewry, D.H., Wells, C.I., Andrews, D.M., Angell, R., Al-Ali, H., Axtman, A.D., Capuzzi, S.J., Elkins,
725 J.M., Ettmayer, P., Frederiksen, M. et al. (2017). Progress towards a public chemogenomic set
726 for protein kinases and a call for contributions. PLoS One 12, e0181585.
727 https://doi.org/10.1371/journal.pone.0181585.
728 5. Zhang, J., Yang, L.P., and Gray, S.N. (2009). Targeting cancer with small molecule kinase
729 inhibitors. Nature Reviews Cancer 9, 28-39. https://doi.org/10.1038/nrc2559.
730 6. Roskoski, R. (2024). Properties of FDA-approved small molecule protein kinase inhibitors: A
731 2024 update. Pharmacological Research 200, 107059.
732 https://doi.org/10.1016/j.phrs.2024.107059.
733 7. Pufall, M.A., and Graves, B.J. (2002). Autoinhibitory domains: modular effectors of cellular
734 regulation. Annu Rev Cell Dev Biol 18, 421-462.
735 https://doi.org/10.1146/annurev.cellbio.18.031502.133614.
736 8. Varjosalo, M., Keskitalo, S., Drogen, V.A., Nurkkala, H., Vichalkovski, A., Aebersold, R., and
737 Gstaiger, M. (2013). The Protein Interaction Landscape of the Human CMGC Kinase Group. Cell
738 Reports 3, 1306-1320. https://doi.org/10.1016/j.celrep.2013.03.027.
739 9. Buljan, M., Ciuffa, R., van Drogen, A., Vichalkovski, A., Mehnert, M., Rosenberger, G., Lee, S.,
740 Varjosalo, M., Pernas, L.E., Spegg, V. et al. (2020). Kinase Interaction Network Expands
741 Functional and Disease Roles of Human Kinases. Mol Cell 79, 504-520 e509.
742 https://doi.org/10.1016/j.molcel.2020.07.001.
743 10. Cho, D., Lee, H.M., Kim, J.A., Song, J.G., Hwang, S.H., Lee, B., Park, J., Tran, K.M., Kim, J., Vo,
744 P.N.L. et al. (2024). Autoinhibited Protein Database: a curated database of autoinhibitory
745 domains and their autoinhibition mechanisms. Database (Oxford) 2024.
746 https://doi.org/10.1093/database/baae085.
747 11. Nussinov, R., and Tsai, C.J. (2013). Allostery in disease and in drug discovery. Cell 153, 293-305.
748 https://doi.org/10.1016/j.cell.2013.03.034.
749 12. Li, M., Rehman, U.A., Liu, Y., Chen, K., and Lu, S. (2021). Dual roles of ATP-binding site in protein
750 kinases: Orthosteric inhibition and allosteric regulation. In Advances in Protein Chemistry and
751 Structural Biology, pp. 87-119. https://doi.org/10.1016/bs.apcsb.2020.09.005.
752 13. Gogl, G., Kornev, A.P., Remenyi, A., and Taylor, S.S. (2019). Disordered Protein Kinase Regions
753 in Regulation of Kinase Domain Cores. Trends Biochem Sci 44, 300-311.
754 https://doi.org/10.1016/j.tibs.2018.12.002.
755 14. Fenton, M., Gregory, E., and Daughdrill, G. (2023). Protein disorder and autoinhibition: The
756 role of multivalency and effective concentration. Curr Opin Struct Biol 83, 102705.
757 https://doi.org/10.1016/j.sbi.2023.102705.
758 15. Li, M., Cao, H., Lai, L., and Liu, Z. (2018). Disordered linkers in multidomain allosteric proteins:
759 Entropic effect to favor the open state or enhanced local concentration to favor the closed
760 state? Protein Sci 27, 1600-1610. https://doi.org/10.1002/pro.3475.
761 16. Roux, J.K., Kim, I.D., Raida, M., and Burke, B. (2012). A promiscuous biotin ligase fusion protein
762 identifies proximal and interacting proteins in mammalian cells. Journal of Cell Biology 196,
763 801-810. https://doi.org/https://doi.org/10.1083/jcb.201112098.

764 17. Lambert, J.-P., Tucholska, M., Go, C., Knight, J.D.R., and Gingras, A.-C. (2015). Proximity
765 biotinylation and affinity purification are complementary approaches for the interactome
766 mapping of chromatin-associated protein complexes. Journal of Proteomics 118, 81-94.
767 https://doi.org/https://doi.org/10.1016/j.jprot.2014.09.011.
768 18. Piazza, I., Beaton, N., Bruderer, R., Knobloch, T., Barbisan, C., Chandat, L., Sudau, A., Siepe, I.,
769 Rinner, O., de Souza, N. et al. (2020). A machine learning-based chemoproteomic approach to
770 identify drug targets and binding sites in complex proteomes. Nat Commun 11, 4200.
771 https://doi.org/10.1038/s41467-020-18071-x.
772 19. Feng, Y., De Franceschi, G., Kahraman, A., Soste, M., Melnik, A., Boersema, P.J., de Laureto,
773 P.P., Nikolaev, Y., Oliveira, A.P., and Picotti, P. (2014). Global analysis of protein structural
774 changes in complex proteomes. Nat Biotechnol 32, 1036-1044.
775 https://doi.org/10.1038/nbt.2999.
776 20. Stalder, P., Serdiuk, T., Ghosh, D., Fleischmann, Y., Ait-Bouziad, N., Quast, J.P., Malinovska, L.,
777 Ouared, A., Davranche, A., Haenseler, W. et al. (2025). An approach to characterize
778 mechanisms of action of anti-amyloidogenic compounds in vitro and in situ. NPJ Parkinsons Dis
779 11, 122. https://doi.org/10.1038/s41531-025-00966-5.
780 21. Holfeld, A., Schuster, D., Sesterhenn, F., Gillingham, A.K., Stalder, P., Haenseler, W., Barrio-
781 Hernandez, I., Ghosh, D., Vowles, J., Cowley, S.A. et al. (2024). Systematic identification of
782 structure-specific protein-protein interactions. Mol Syst Biol 20, 651-675.
783 https://doi.org/10.1038/s44320-024-00037-6.
784 22. Ferguson, F.M., Nabet, B., Raghavan, S., Liu, Y., Leggett, A.L., Kuljanin, M., Kalekar, R.L., Yang,
785 A., He, S., Wang, J. et al. (2020). Discovery of a selective inhibitor of doublecortin like kinase 1.
786 Nat Chem Biol 16, 635-643. https://doi.org/10.1038/s41589-020-0506-0.
787 23. Patel, O., Roy, M.J., Kropp, A., Hardy, J.M., Dai, W., and Lucet, I.S. (2021). Structural basis for
788 small molecule targeting of Doublecortin Like Kinase 1 with DCLK1-IN-1. Commun Biol 4, 1105.
789 https://doi.org/10.1038/s42003-021-02631-y.
790 24. Cheng, L., Yang, Z., Guo, W., Wu, C., Liang, S., Tong, A., Cao, Z., Thorne, R.F., Yang, S.Y., Yu, Y.
791 et al. (2022). DCLK1 autoinhibition and activation in tumorigenesis. Innovation (Camb) 3,
792 100191. https://doi.org/10.1016/j.xinn.2021.100191.
793 25. Kylarova, S., Psenakova, K., Herman, P., Obsilova, V., and Obsil, T. (2018). CaMKK2 kinase
794 domain interacts with the autoinhibitory region through the N-terminal lobe including the RP
795 insert. Biochimica et Biophysica Acta (BBA) - General Subjects 1862, 2304-2313.
796 https://doi.org/10.1016/j.bbagen.2018.07.025.
797 26. Katsuragi, Y., and Sagata, N. (2004). Regulation of Chk1 kinase by autoinhibition and ATR-
798 mediated phosphorylation. Mol Biol Cell 15, 1680-1689. https://doi.org/10.1091/mbc.e03-12-
799 0874.
800 27. House, C., and Kemp, B.E. (1987). Protein kinase C contains a pseudosubstrate prototope in its
801 regulatory domain. Science 238, 1726-1728. https://doi.org/10.1126/science.3686012.
802 28. Sommese, R.F., Ritt, M., Swanson, C.J., and Sivaramakrishnan, S. (2017). The Role of Regulatory
803 Domains in Maintaining Autoinhibition in the Multidomain Kinase PKCalpha. J Biol Chem 292,
804 2873-2880. https://doi.org/10.1074/jbc.M116.768457.
805 29. Wells, C., Liang, Y., Pulliam, T.L., Lin, C., Awad, D., Eduful, B., O'Byrne, S., Hossain, M.A., Catta-
806 Preta, C.M.C., Ramos, P.Z. et al. (2023). SGC-CAMKK2-1: A Chemical Probe for CAMKK2. Cells
807 12, 287. https://doi.org/10.3390/cells12020287.

808 30. King, C., Diaz, H., Barnard, D., Barda, D., Clawson, D., Blosser, W., Cox, K., Guo, S., and Marshall,
809 M. (2014). Characterization and preclinical development of LY2603618: a selective and potent
810 Chk1 inhibitor. Invest New Drugs 32, 213-226. https://doi.org/10.1007/s10637-013-0036-7.
811 31. Frings, S. (1993). Protein kinase C sensitizes olfactory adenylate cyclase. J Gen Physiol 101, 183-
812 205. https://doi.org/10.1085/jgp.101.2.183.
813 32. Rotenberg, S.A., Zhu, J., Hansen, H., Li, X.D., Sun, X.G., Michels, C.A., and Riedel, H. (1998).
814 Deletion analysis of protein kinase Calpha reveals a novel regulatory segment. J Biochem 124,
815 756-763. https://doi.org/10.1093/oxfordjournals.jbchem.a022176.
816 33. Han, X., Tang, J., Wang, J., Ren, F., Zheng, J., Gragg, M., Kiser, P., Park, S.H.P., Palczewski, K.,
817 Yao, X. et al. (2016). Conformational Change of Human Checkpoint Kinase 1 (Chk1) Induced by
818 DNA Damage. Journal of Biological Chemistry 291, 12951-12959.
819 https://doi.org/10.1074/jbc.M115.713248.
820 34. Orr, J.W., and Newton, A.C. (1994). Intrapeptide regulation of protein kinase C. J Biol Chem
821 269, 8383-8387.
822 35. Orr, J.W., Keranen, L.M., and Newton, A.C. (1992). Reversible exposure of the pseudosubstrate
823 domain of protein kinase C by phosphatidylserine and diacylglycerol. J Biol Chem 267, 15263-
824 15266.
825 36. Antal, C.E., Violin, J.D., Kunkel, M.T., Skovso, S., and Newton, A.C. (2014). Intramolecular
826 conformational changes optimize protein kinase C signaling. Chem Biol 21, 459-469.
827 https://doi.org/10.1016/j.chembiol.2014.02.008.
828 37. Endicott, J.A., Noble, M.E., and Johnson, L.N. (2012). The structural basis for control of
829 eukaryotic protein kinases. Annu Rev Biochem 81, 587-613. https://doi.org/10.1146/annurev-
830 biochem-052410-090317.
831 38. Oughtred, R., Rust, J., Chang, C., Breitkreutz, B.J., Stark, C., Willems, A., Boucher, L., Leung, G.,
832 Kolas, N., Zhang, F. et al. (2021). The BioGRID database: A comprehensive biomedical resource
833 of curated protein, genetic, and chemical interactions. Protein Sci 30, 187-200.
834 https://doi.org/10.1002/pro.3978.
835 39. Woods, A., Dickerson, K., Heath, R., Hong, S.P., Momcilovic, M., Johnstone, S.R., Carlson, M.,
836 and Carling, D. (2005). Ca2+/calmodulin-dependent protein kinase kinase-beta acts upstream
837 of AMP-activated protein kinase in mammalian cells. Cell Metab 2, 21-33.
838 https://doi.org/10.1016/j.cmet.2005.06.005.
839 40. Anderson, K.A., Ribar, T.J., Lin, F., Noeldner, P.K., Green, M.F., Muehlbauer, M.J., Witters, L.A.,
840 Kemp, B.E., and Means, A.R. (2008). Hypothalamic CaMKK2 contributes to the regulation of
841 energy balance. Cell Metab 7, 377-388. https://doi.org/10.1016/j.cmet.2008.02.011.
842 41. Green, M.F., Anderson, K.A., and Means, A.R. (2011). Characterization of the CaMKKbeta-
843 AMPK signaling complex. Cell Signal 23, 2005-2012.
844 https://doi.org/10.1016/j.cellsig.2011.07.014.
845 42. Wells, C., Liang, Y., Pulliam, L.T., Lin, C., Awad, D., Eduful, B., O'Byrne, S., Hossain, A.M., Catta-
846 Preta, C.M.C., Ramos, Z.P. et al. (2023). SGC-CAMKK2-1: A Chemical Probe for CAMKK2. Cells
847 12, 287. https://doi.org/10.3390/cells12020287.
848 43. Green, M.F., Scott, J.W., Steel, R., Oakhill, J.S., Kemp, B.E., and Means, A.R. (2011).
849 Ca2+/Calmodulin-dependent protein kinase kinase beta is regulated by multisite
850 phosphorylation. J Biol Chem 286, 28066-28079. https://doi.org/10.1074/jbc.M111.251504.
851 44. Xy Ling, N., Langendorf, C.G., Hoque, A., Galic, S., Loh, K., Kemp, B.E., Gundlach, A.L., Oakhill,
852 J.S., and Scott, J.W. (2020). Functional analysis of an R311C variant of Ca(2+) -calmodulin-

853 dependent protein kinase kinase-2 (CaMKK2) found as a de novo mutation in a patient with
854 bipolar disorder. Bipolar Disord 22, 841-848. https://doi.org/10.1111/bdi.12901.
855 45. Tokumitsu, H., Hatano, N., Fujimoto, T., Yurimoto, S., and Kobayashi, R. (2011). Generation of
856 autonomous activity of Ca(2+)/calmodulin-dependent protein kinase kinase beta by
857 autophosphorylation. Biochemistry 50, 8193-8201. https://doi.org/10.1021/bi201005g.
858 46. Ishikawa, Y., Tokumitsu, H., Inuzuka, H., Murata-Hori, M., Hosoya, H., and Kobayashi, R. (2003).
859 Identification and characterization of novel components of a Ca2+/calmodulin-dependent
860 protein kinase cascade in HeLa cells. FEBS Lett 550, 57-63. https://doi.org/10.1016/s0014-
861 5793(03)00817-2.
862 47. Abramson, J., Adler, J., Dunger, J., Evans, R., Green, T., Pritzel, A., Ronneberger, O., Willmore,
863 L., Ballard, A.J., Bambrick, J. et al. (2024). Accurate structure prediction of biomolecular
864 interactions with AlphaFold 3. Nature 630, 493-500. https://doi.org/10.1038/s41586-024-
865 07487-w.
866 48. Shaw, R.J., Lamia, K.A., Vasquez, D., Koo, S.H., Bardeesy, N., Depinho, R.A., Montminy, M., and
867 Cantley, L.C. (2005). The kinase LKB1 mediates glucose homeostasis in liver and therapeutic
868 effects of metformin. Science 310, 1642-1646. https://doi.org/10.1126/science.1120781.
869 49. Jiang, K., Pereira, E., Maxfield, M., Russell, B., Goudelock, D.M., and Sanchez, Y. (2003).
870 Regulation of Chk1 includes chromatin association and 14-3-3 binding following
871 phosphorylation on Ser-345. J Biol Chem 278, 25207-25217.
872 https://doi.org/10.1074/jbc.M300070200.
873 50. Alonso-de Vega, I., Martin, Y., and Smits, V.A. (2014). USP7 controls Chk1 protein stability by
874 direct deubiquitination. Cell Cycle 13, 3921-3926.
875 https://doi.org/10.4161/15384101.2014.973324.
876 51. Zhang, P., Wei, Y., Wang, L., Debeb, B.G., Yuan, Y., Zhang, J., Yuan, J., Wang, M., Chen, D., Sun,
877 Y. et al. (2014). ATM-mediated stabilization of ZEB1 promotes DNA damage response and
878 radioresistance through CHK1. Nat Cell Biol 16, 864-875. https://doi.org/10.1038/ncb3013.
879 52. Scorah, J., Dong, M.Q., Yates, J.R., 3rd, Scott, M., Gillespie, D., and McGowan, C.H. (2008). A
880 conserved proliferating cell nuclear antigen-interacting protein sequence in Chk1 is required
881 for checkpoint function. J Biol Chem 283, 17250-17259.
882 https://doi.org/10.1074/jbc.M800369200.
883 53. Han, X., Aslanian, A., Fu, K., Tsuji, T., and Zhang, Y. (2014). The Interaction between Checkpoint
884 Kinase 1 (Chk1) and the Minichromosome Maintenance (MCM) Complex Is Required for DNA
885 Damage-induced Chk1 Phosphorylation. Journal of Biological Chemistry 289, 24716-24723.
886 https://doi.org/https://doi.org/10.1074/jbc.M114.575035.
887 54. Liu, S., Bekker-Jensen, S., Mailand, N., Lukas, C., Bartek, J., and Lukas, J. (2006). Claspin
888 operates downstream of TopBP1 to direct ATR signaling towards Chk1 activation. Mol Cell Biol
889 26, 6056-6064. https://doi.org/10.1128/MCB.00492-06.
890 55. Leung-Pineda, V., Ryan, C.E., and Piwnica-Worms, H. (2006). Phosphorylation of Chk1 by ATR
891 is antagonized by a Chk1-regulated protein phosphatase 2A circuit. Mol Cell Biol 26, 7529-
892 7538. https://doi.org/10.1128/MCB.00447-06.
893 56. Booth, L., Cruickshanks, N., Ridder, T., Dai, Y., Grant, S., and Dent, P. (2013). PARP and CHK
894 inhibitors interact to cause DNA damage and cell death in mammary carcinoma cells. Cancer
895 Biol Ther 14, 458-465. https://doi.org/10.4161/cbt.24424.
896 57. Okita, N., Minato, S., Ohmi, E., Tanuma, S., and Higami, Y. (2012). DNA damage-induced CHK1
897 autophosphorylation at Ser296 is regulated by an intramolecular mechanism. FEBS Lett 586,
898 3974-3979. https://doi.org/10.1016/j.febslet.2012.09.048.

899 58. Kasahara, K., Goto, H., Enomoto, M., Tomono, Y., Kiyono, T., and Inagaki, M. (2010). 14-3-
900 3gamma mediates Cdc25A proteolysis to block premature mitotic entry after DNA damage.
901 EMBO J 29, 2802-2812. https://doi.org/10.1038/emboj.2010.157.
902 59. Antonicka, H., Lin, Z.Y., Janer, A., Aaltonen, M.J., Weraarpachai, W., Gingras, A.C., and
903 Shoubridge, E.A. (2020). A High-Density Human Mitochondrial Proximity Interaction Network.
904 Cell Metab 32, 479-497. https://doi.org/10.1016/j.cmet.2020.07.017.
905 60. Golkowski, M., Lius, A., Sapre, T., Lau, H.T., Moreno, T., Maly, D.J., and Ong, S.E. (2023).
906 Multiplexed kinase interactome profiling quantifies cellular network activity and plasticity. Mol
907 Cell 83, 803-818. https://doi.org/10.1016/j.molcel.2023.01.015.
908 61. Wang, J., Han, X., and Zhang, Y. (2012). Autoregulatory Mechanisms of Phosphorylation of
909 Checkpoint Kinase 1. Cancer Research 72, 3786-3794. https://doi.org/10.1158/0008-
910 5472.CAN-12-0523.
911 62. D'Angelo, D., Sanchez-Vazquez, V.H., Cartes-Saavedra, B., Vecellio Reane, D., Cupo, R.R.,
912 Delgado de la Herran, H., Ghirardo, G., Shorter, J., Wevers, R.A., Wortmann, S.B. et al. (2025).
913 Dependence of mitochondrial calcium signalling and dynamics on the disaggregase, CLPB. Nat
914 Commun 16, 2810. https://doi.org/10.1038/s41467-025-57641-9.
915 63. Wiemerslage, L., and Lee, D. (2016). Quantification of mitochondrial morphology in neurites of
916 dopaminergic neurons using multiple parameters. Journal of Neuroscience Methods 262, 56-
917 65. https://doi.org/https://doi.org/10.1016/j.jneumeth.2016.01.008.
918 64. Shami, J.G., Cheng, D., Verhaegh, P., Koek, G., Wisse, E., and Braet, F. (2021). Three-
919 dimensional ultrastructure of giant mitochondria in human non-alcoholic fatty liver disease.
920 Scientific Reports 11. https://doi.org/https://doi.org/10.1038/s41598-021-82884-z.
921 65. Sanchez, Y., Wong, C., Thoma, R.S., Richman, R., Wu, Z., Piwnica-Worms, H., and Elledge, S.J.
922 (1997). Conservation of the Chk1 Checkpoint Pathway in Mammals: Linkage of DNA Damage
923 to Cdk Regulation Through Cdc25. Science 277, 1497-1501.
924 https://doi.org/https://doi.org/10.1126/science.277.5331.1497.
925 66. Taguchi, N., Ishihara, N., Jofuku, A., Oka, T., and Mihara, K. (2007). Mitotic phosphorylation of
926 dynamin-related GTPase Drp1 participates in mitochondrial fission. J Biol Chem 282, 11521-
927 11529. https://doi.org/10.1074/jbc.M607279200.
928 67. Horbay, R., and Bilyy, R. (2016). Mitochondrial dynamics during cell cycling. Apoptosis 21,
929 1327-1335. https://doi.org/https://doi.org/10.1007/s10495-016-1295-5.
930 68. Ng, T., Shima, D., Squire, A., Bastiaens, P.I., Gschmeissner, S., Humphries, M.J., and Parker, P.J.
931 (1999). PKCalpha regulates beta1 integrin-dependent cell motility through association and
932 control of integrin traffic. EMBO J 18, 3909-3923. https://doi.org/10.1093/emboj/18.14.3909.
933 69. Medkova, M., and Cho, W. (1998). Mutagenesis of the C2 domain of protein kinase C-alpha.
934 Differential roles of Ca2+ ligands and membrane binding residues. J Biol Chem 273, 17544-
935 17552. https://doi.org/10.1074/jbc.273.28.17544.
936 70. Ueda, Y., Hirai, S., Osada, S., Suzuki, A., Mizuno, K., and Ohno, S. (1996). Protein kinase C
937 activates the MEK-ERK pathway in a manner independent of Ras and dependent on Raf. J Biol
938 Chem 271, 23512-23519. https://doi.org/10.1074/jbc.271.38.23512.
939 71. Stamatovic, M.S., Johnson, M.A., Sladojevic, N., Keep, F.R., and Andjelkovic, V.A. (2017).
940 Endocytosis of tight junction proteins and the regulation of degradation and recycling. Annals
941 of the New York Academy of Sciences 1397, 54-65.
942 https://doi.org/https://doi.org/10.1111/nyas.13346.

943 72. Evans, J.H., Murray, D., Leslie, C.C., and Falke, J.J. (2006). Specific translocation of protein
944 kinase Calpha to the plasma membrane requires both Ca2+ and PIP2 recognition by its C2
945 domain. Mol Biol Cell 17, 56-66. https://doi.org/10.1091/mbc.e05-06-0499.
946 73. Nolen, B., Taylor, S., and Ghosh, G. (2004). Regulation of Protein Kinases. Molecular Cell 15,
947 661-675. https://doi.org/10.1016/j.molcel.2004.08.024.
948 74. Matthews, T.P., Jones, A.M., and Collins, I. (2013). Structure-based design, discovery and
949 development of checkpoint kinase inhibitors as potential anticancer therapies. Expert Opinion
950 on Drug Discovery 8, 621-640.
951 https://doi.org/https://doi.org/10.1517/17460441.2013.788496.
952 75. Gould, C.M., Antal, C.E., Reyes, G., Kunkel, M.T., Adams, R.A., Ziyar, A., Riveros, T., and Newton,
953 A.C. (2011). Active Site Inhibitors Protect Protein Kinase C from Dephosphorylation and
954 Stabilize Its Mature Form. Journal of Biological Chemistry 286, 28922-28930.
955 https://doi.org/https://doi.org/10.1074/jbc.M111.272526.
956 76. Cupo, R.R., and Shorter, J. (2020). Skd3 (human ClpB) is a potent mitochondrial protein
957 disaggregase that is inactivated by 3-methylglutaconic aciduria-linked mutations. Elife 9.
958 https://doi.org/10.7554/eLife.55279.
959 77. Huttlin, E.L., Bruckner, R.J., Navarrete-Perea, J., Cannon, J.R., Baltier, K., Gebreab, F., Gygi,
960 M.P., Thornock, A., Zarraga, G., Tam, S. et al. (2021). Dual proteome-scale networks reveal cell-
961 specific remodeling of the human interactome. Cell 184, 3022-3040 e3028.
962 https://doi.org/10.1016/j.cell.2021.04.011.
963 78. Chen, X., Glytsou, C., Zhou, H., Narang, S., Reyna, D.E., Lopez, A., Sakellaropoulos, T., Gong, Y.,
964 Kloetgen, A., Yap, Y.S. et al. (2019). Targeting Mitochondrial Structure Sensitizes Acute Myeloid
965 Leukemia to Venetoclax Treatment. Cancer Discov 9, 890-909. https://doi.org/10.1158/2159-
966 8290.CD-19-0117.
967 79. Han, Y., Chen, Y.S., Liu, Z., Bodyak, N., Rigor, D., Bisping, E., Pu, W.T., and Kang, P.M. (2006).
968 Overexpression of HAX-1 protects cardiac myocytes from apoptosis through caspase-9
969 inhibition. Circ Res 99, 415-423. https://doi.org/10.1161/01.RES.0000237387.05259.a5.
970 80. Duvezin-Caubet, S., Jagasia, R., Wagener, J., Hofmann, S., Trifunovic, A., Hansson, A., Chomyn,
971 A., Bauer, M.F., Attardi, G., Larsson, N.-G. et al. (2006). Proteolytic Processing of OPA1 Links
972 Mitochondrial Dysfunction to Alterations in Mitochondrial Morphology. Journal of Biological
973 Chemistry 281, 37972-37979. https://doi.org/https://doi.org/10.1074/jbc.M606059200.
974 81. Parissenti, A.M., Kirwan, A.F., Kim, S.A., Colantonio, C.M., and Schimmer, B.P. (1998). Inhibitory
975 properties of the regulatory domains of human protein kinase Calpha and mouse protein
976 kinase Cepsilon. J Biol Chem 273, 8940-8945. https://doi.org/10.1074/jbc.273.15.8940.
977 82. Ono, Y., Fujii, T., Igarashi, K., Kuno, T., Tanaka, C., Kikkawa, U., and Nishizuka, Y. (1989). Phorbol
978 ester binding to protein kinase C requires a cysteine-rich zinc-finger-like sequence. Proc Natl
979 Acad Sci U S A 86, 4868-4871. https://doi.org/10.1073/pnas.86.13.4868.
980 83. Verdaguer, N., Corbalan-Garcia, S., Ochoa, W.F., Fita, I., and Gomez-Fernandez, J.C. (1999).
981 Ca(2+) bridges the C2 membrane-binding domain of protein kinase Calpha directly to
982 phosphatidylserine. EMBO J 18, 6329-6338. https://doi.org/10.1093/emboj/18.22.6329.
983 84. Sanchez-Bautista, S., Marin-Vicente, C., Gomez-Fernandez, J.C., and Corbalan-Garcia, S. (2006).
984 The C2 domain of PKCalpha is a Ca2+ -dependent PtdIns(4,5)P2 sensing domain: a new insight
985 into an old pathway. J Mol Biol 362, 901-914. https://doi.org/10.1016/j.jmb.2006.07.093.
986 85. Martin-Belmonte, F., Gassama, A., Datta, A., Yu, W., Rescher, U., Gerke, V., and Mostov, K.
987 (2007). PTEN-mediated apical segregation of phosphoinositides controls epithelial
988 morphogenesis through Cdc42. Cell 128, 383-397. https://doi.org/10.1016/j.cell.2006.11.051.

989 86. Roskoski, R., Jr. (2026). Properties of FDA-approved small molecule protein kinase inhibitors:
990 A 2026 update. Pharmacol Res 224, 108107. https://doi.org/10.1016/j.phrs.2026.108107.
991 87. Gorantla, S.P., Oelschlager, L., Prince, G., Osius, J., Kolluri, S.B., Maluje, Y., Fahnrich, A., Ernst,
992 N., Barbosa Gulde, A., Ludwig, R.J. et al. (2025). Ruxolitinib mediated paradoxical JAK2
993 hyperphosphorylation is due to the protection of activation loop tyrosines from phosphatases.
994 Leukemia 39, 1678-1691. https://doi.org/10.1038/s41375-025-02594-7.
995 88. Gurevic, I., Meudec, L., Mariette, X., Nocturne, G., and McCoy, S.S. (2025). JAK inhibitor
996 withdrawal causes a transient pro-inflammatory cascade: A potential mechanism for major
997 adverse cardiac events. PLoS One 20, e0311706.
998 https://doi.org/10.1371/journal.pone.0311706.
999 89. Hatzivassiliou, G., Song, K., Yen, I., Brandhuber, B.J., Anderson, D.J., Alvarado, R., Ludlam, M.J.,
1000 Stokoe, D., Gloor, S.L., Vigers, G. et al. (2010). RAF inhibitors prime wild-type RAF to activate
1001 the MAPK pathway and enhance growth. Nature 464, 431-435.
1002 https://doi.org/10.1038/nature08833.
1003 90. Haling, J.R., Sudhamsu, J., Yen, I., Sideris, S., Sandoval, W., Phung, W., Bravo, B.J., Giannetti,
1004 A.M., Peck, A., Masselot, A. et al. (2014). Structure of the BRAF-MEK complex reveals a kinase
1005 activity independent role for BRAF in MAPK signaling. Cancer Cell 26, 402-413.
1006 https://doi.org/10.1016/j.ccr.2014.07.007.
1007 91. Stewart, H.I., Grinfeld, D., Giannakopulos, A., Petzoldt, J., Shanley, T., Garland, M., Denisov, E.,
1008 Peterson, A.C., Damoc, E., Zeller, M. et al. (2023). Parallelized Acquisition of Orbitrap and Astral
1009 Analyzers Enables High-Throughput Quantitative Analysis. Anal Chem 95, 15656-15664.
1010 https://doi.org/10.1021/acs.analchem.3c02856.
1011 92. Glatter, T., Wepf, A., Aebersold, R., and Gstaiger, M. (2009). An integrated workflow for
1012 charting the human interaction proteome: insights into the PP2A system. Mol Syst Biol 5, 237.
1013 https://doi.org/10.1038/msb.2008.75.
1014 93. Collaboration, T.O. (2016). The ORFeome Collaboration: a genome-scale human ORF-clone
1015 resource. Nature Methods 13, 191-192. https://doi.org/10.1038/nmeth.3776.
1016 94. Varjosalo, M., Bjorklund, M., Cheng, F., Syvanen, H., Kivioja, T., Kilpinen, S., Sun, Z., Kallioniemi,
1017 O., Stunnenberg, H.G., He, W.W. et al. (2008). Application of active and kinase-deficient
1018 kinome collection for identification of kinases regulating hedgehog signaling. Cell 133, 537-
1019 548. https://doi.org/10.1016/j.cell.2008.02.047.
1020 95. Liu, X., Salokas, K., Weldatsadik, R.G., Gawriyski, L., and Varjosalo, M. (2020). Combined
1021 proximity labeling and affinity purification-mass spectrometry workflow for mapping and
1022 visualizing protein interaction networks. Nat Protoc 15, 3182-3211.
1023 https://doi.org/10.1038/s41596-020-0365-x.
1024 96. Reber, V., and Gstaiger, M. (2023). Target Deconvolution by Limited Proteolysis Coupled to
1025 Mass Spectrometry. Methods Mol Biol 2706, 177-190. https://doi.org/10.1007/978-1-0716-
1026 3397-7_13.
1027 97. Rafiee, M.R., Sigismondo, G., Kalxdorf, M., Forster, L., Brugger, B., Bethune, J., and Krijgsveld,
1028 J. (2020). Protease-resistant streptavidin for interaction proteomics. Mol Syst Biol 16, e9370.
1029 https://doi.org/10.15252/msb.20199370.
1030 98. Quast, J.P., Schuster, D., and Picotti, P. (2022). protti: an R package for comprehensive data
1031 analysis of peptide- and protein-centric bottom-up proteomics data. Bioinform Adv 2,
1032 vbab041. https://doi.org/10.1093/bioadv/vbab041.
1033 99. Brombacher, E., Schad, A., and Kreutz, C. (2020). Tail-Robust Quantile Normalization.
1034 Proteomics 20, e2000068. https://doi.org/10.1002/pmic.202000068.

100. Ritchie, M.E., Phipson, B., Wu, D., Hu, Y., Law, C.W., Shi, W., and Smyth, G.K. (2015). limma powers differential expression analyses for RNA-sequencing and microarray studies. Nucleic Acids Res 43, e47. https://doi.org/10.1093/nar/gkv007.
101. Benjamini, Y., and Hochberg, Y. (1995). Controlling the False Discovery Rate: A Practical and Powerful Approach to Multiple Testing. Journal of the Royal Statistical Society Series B: Statistical Methodology 57, 289-300. https://doi.org/10.1111/j.2517-6161.1995.tb02031.x.
102. Cox, J., Hein, M.Y., Luber, C.A., Paron, I., Nagaraj, N., and Mann, M. (2014). Accurate proteome-wide label-free quantification by delayed normalization and maximal peptide ratio extraction, termed MaxLFQ. Mol Cell Proteomics 13, 2513-2526. https://doi.org/10.1074/mcp.M113.031591.
103. Sowa, M.E., Bennett, E.J., Gygi, S.P., and Harper, J.W. (2009). Defining the human deubiquitinating enzyme interaction landscape. Cell 138, 389-403. https://doi.org/10.1016/j.cell.2009.04.042.
104. Hediyeh-Zadeh, S., Webb, A.I., and Davis, M.J. (2023). MsImpute: Estimation of Missing Peptide Intensity Data in Label-Free Quantitative Mass Spectrometry. Mol Cell Proteomics 22, 100558. https://doi.org/10.1016/j.mcpro.2023.100558.
105. Berg, S., Kutra, D., Kroeger, T., Straehle, C.N., Kausler, B.X., Haubold, C., Schiegg, M., Ales, J., Beier, T., Rudy, M. et al. (2019). ilastik: interactive machine learning for (bio)image analysis. Nature Methods 16, 1226-1232. https://doi.org/https://doi.org/10.1038/s41592-019-0582-9.
106. Perez-Riverol, Y., Bai, J., Bandla, C., García-Seisdedos, D., Hewapathirana, S., Kamatchinathan, S., Kundu, D.J., Prakash, A., Frericks-Zipper, A., Eisenacher, M. et al. (2022). The PRIDE database resources in 2022: a hub for mass spectrometry-based proteomics evidences. Nucleic Acids Research 50, D543-D552. https://doi.org/https://doi.org/10.1093/nar/gkab1038.

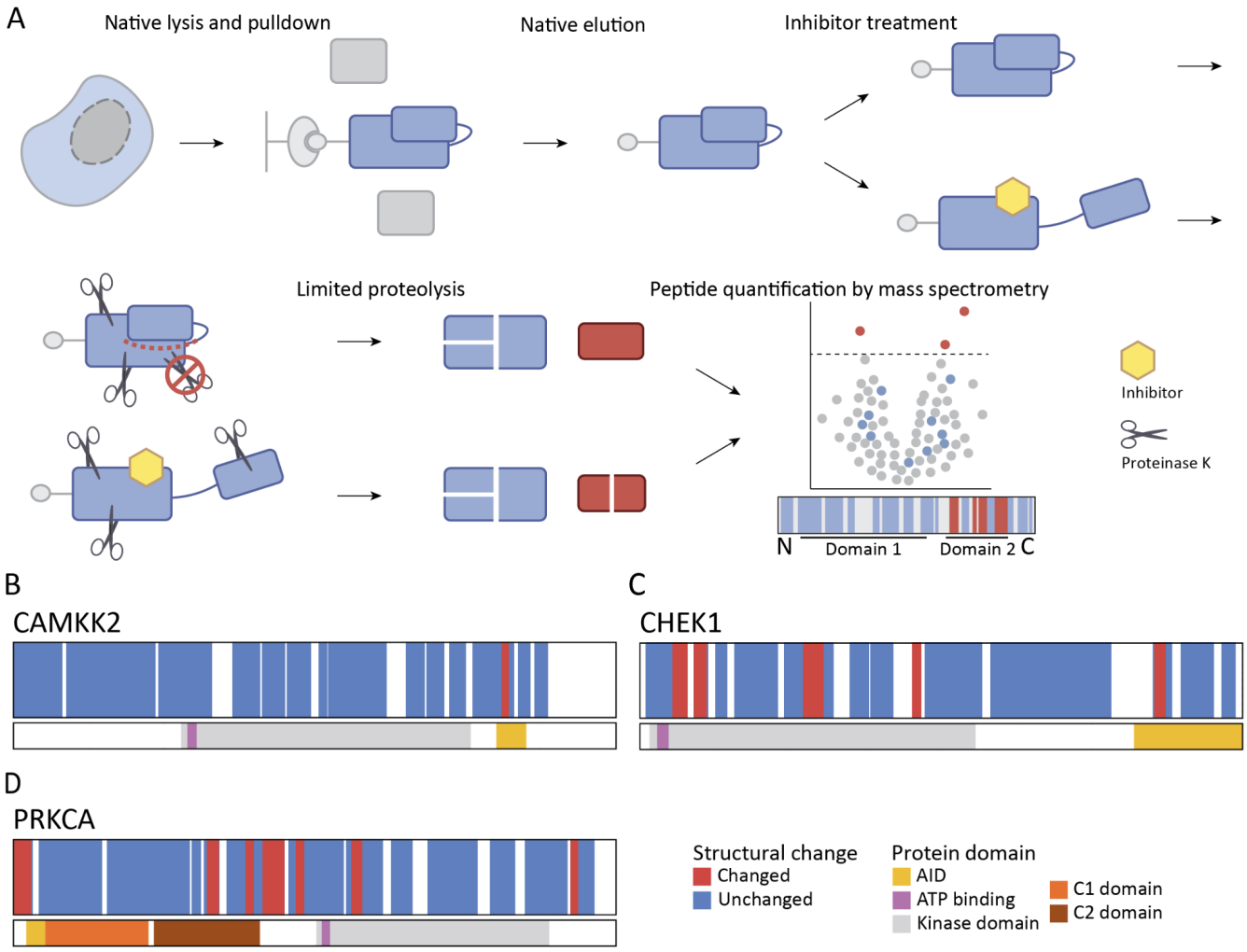

Fig. 1. AP-LiP-MS analysis reveals ATP-competitive inhibition-induced structural changes in kinase AIDs. A) Overview of the AP-LiP-MS workflow. Proteins were lysed and eluted under native conditions before the corresponding inhibitor was added. Following limited proteolysis with PK, the conformation-specific protein fragments were further digested with trypsin under denaturing conditions. Finally, peptides were measured by LC-MS/MS and compared across conditions. B-D) Structural changes observed with AP-LiP-MS for CAMKK2 treated with SGC-CAMKK2-1, CHEK1 treated with rabusertib, and PRKCA treated with Gö 6983. In red are significantly changing peptides, in blue are the non-changing peptides. All AP-LiP-MS experiments were performed in triplicates and p-values were calculated using a moderated t-test followed by multiple testing corrections using the procedure of Benjamini-Hochberg.

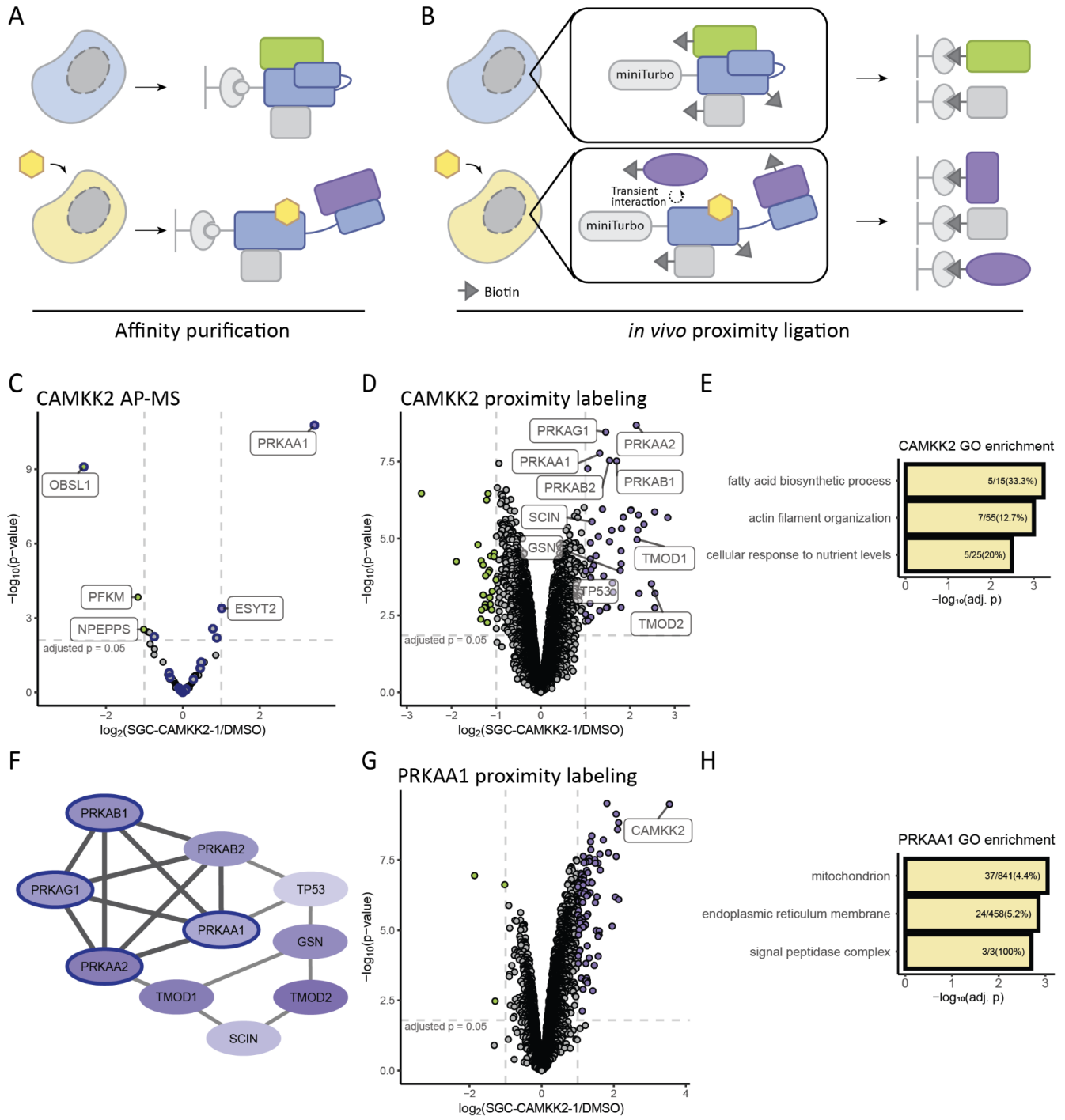

Fig. 2. Binding of the inhibitor SGC-CAMKK2-1 changes CAMKK2 complex formation and proximity. A) Illustration of the AP-MS workflow. B) Illustration of the *in vivo* proximity labeling workflow. C) Volcano plot illustrating changes in CAMKK2 interactors upon inhibition with SGC-CAMKK2-1 measured by AP-MS. Known CAMKK2 interactors are highlighted with a blue border. P-values were calculated using a moderated t-test followed by multiple testing corrections using the procedure of Benjamini-Hochberg. D) Changes in the proximity of CAMKK2 upon inhibition with SGC-CAMKK2-1. P-values were calculated using a moderated t-test followed by multiple testing corrections using the procedure of Benjamini-Hochberg. E) GO enrichment analysis (biological process) of the significantly changing proteins in panel D. P-values were calculated using a Fisher's exact test followed by multiple testing corrections using the procedure of Benjamini-Hochberg. F) PPI network showing the subunits of AMPK complexes and highly interconnected interactors that are significantly increased in the proximity of CAMKK2 upon treatment with SGC-CAMKK2-1 shown in panel D. The AMPK subunit interactions are highlighted with darker edges, and known interactors of CAMKK2 are outlined in blue. G) Reciprocal *in vivo* proximity labeling data showing changes in PRKAA1 proximity upon CAMKK2 inhibition. P-values were calculated using a moderated t-test followed by multiple testing

corrections using the procedure of Benjamini-Hochberg. H) GO enrichment analysis (cellular component) of the significantly changing proteins in panel G. P-values were calculated using a Fisher's exact test followed by multiple testing corrections using the procedure of Benjamini-Hochberg. AP-MS experiments were performed in triplicates, and *in vivo* proximity labeling experiments in quadruplicates.

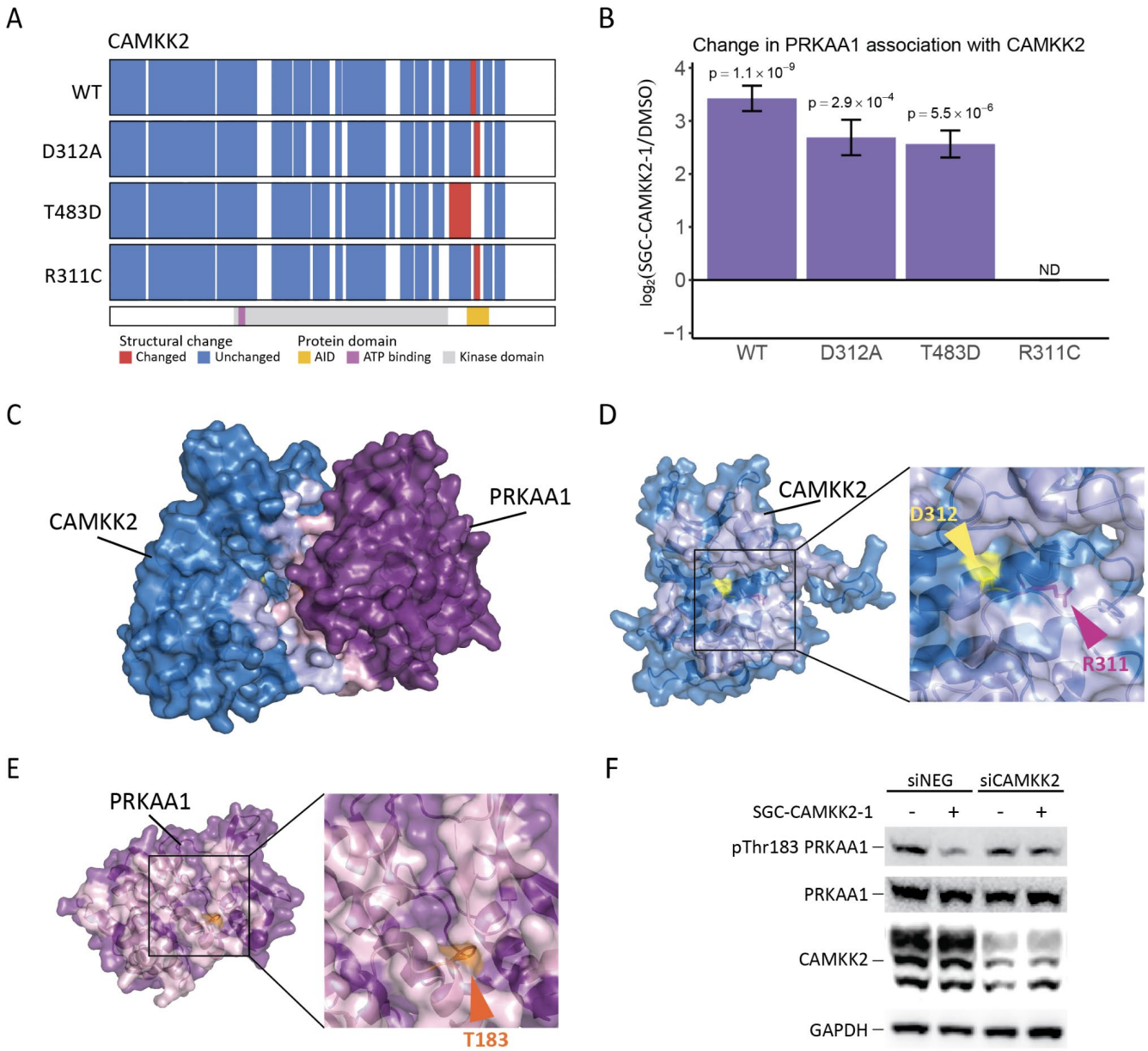

Fig. 3. Inhibitor-induced CAMKK2-PRKAA1 complex formation can attenuate T183 phosphorylation of PRKAA1 by other kinases. A) Comparison of structural changes in CAMKK2 mutants upon SGC-CAMKK2-1 treatment as measured by AP-LiP-MS. B) Bar graph representing $\log_2$(fold change) in PRKAA1 association with CAMKK2 wildtype and indicated mutants following SGC-CAMKK2-1 treatment as measured by AP-MS. Error bars represent the standard error of the mean of the $\log_2$(fold change). C) Predicted structure of the CAMKK2-PRKAA1 complex. CAMKK2 is shown in blue, and PRKAA1 is shown in purple and the predicted interfaces are highlighted in light blue and pink, respectively. Only kinase domains were used in the prediction. D) An up-close view of R311 and D312 of CAMKK2 at the CAMKK2-PRKAA1 interface. R311 is shown in magenta, and D312 is shown in yellow. The predicted interface is highlighted in light blue. E) The predicted PRKAA1 interface in the CAMKK2-PRKAA1 complex. The residue T183 is shown in orange, the predicted interface highlighted in pink. F) Western blot of PRKAA1 phosphorylation in response to CAMKK2 inhibition or siRNA mediated CAMKK2 knockdown. HEK293 cells were treated with control siRNA (siNEG) or siCAMKK2 for 48 hours and vehicle control or SGC-CAMKK2-1 for 4 hours as indicated. Cells were then subjected to glucose starvation for 20 minutes to induce T183 phosphorylation on PRKAA1. AP-LiP-MS and AP-MS experiments were performed in triplicates. P-values were calculated using a moderated t-test followed by multiple testing corrections using the procedure of Benjamini-Hochberg.

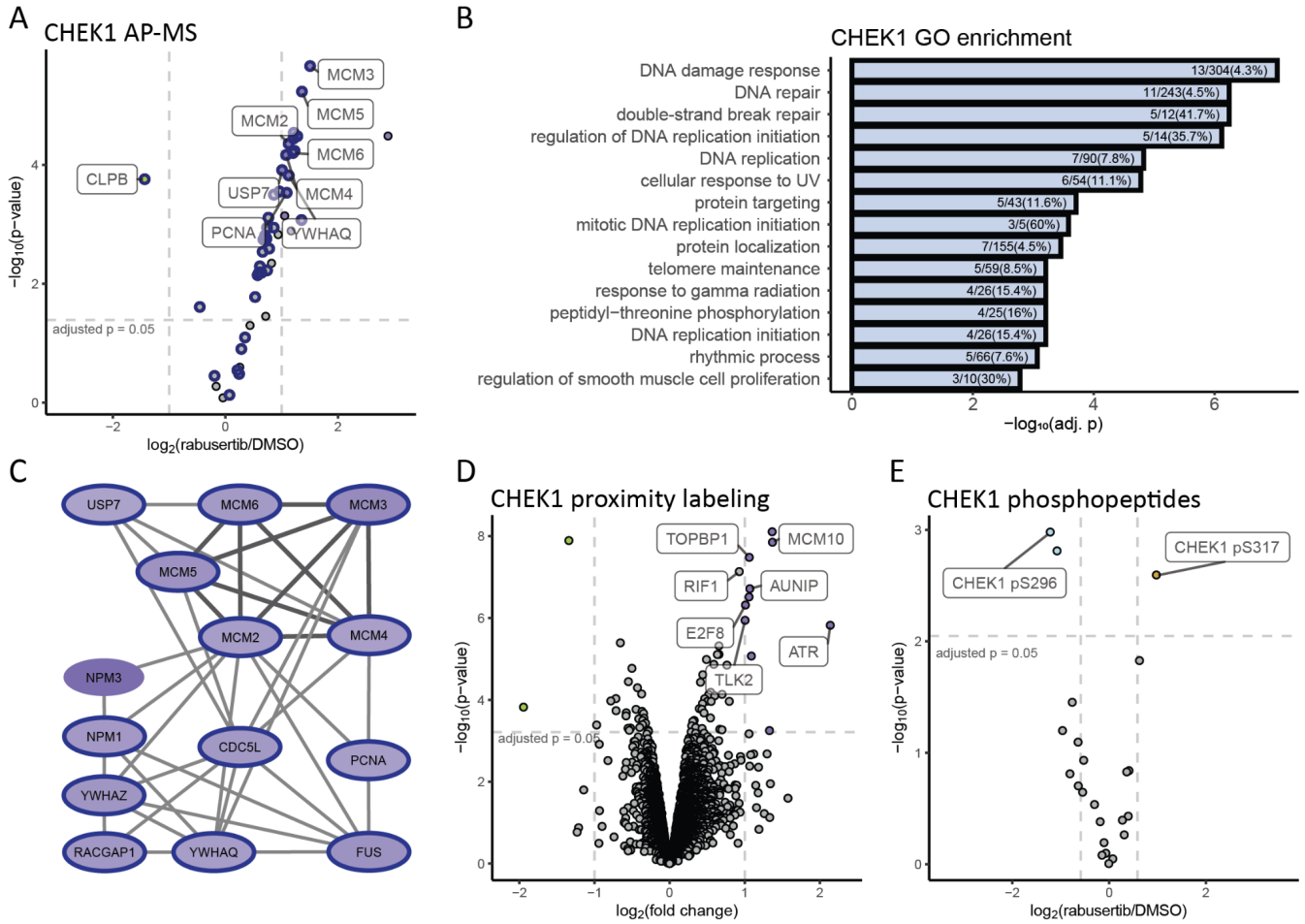

Fig. 4. CHEK1 inhibition with rabusertib alters its interaction with multiple DNA-damage response proteins. A) Volcano plot illustrating changes in abundance of CHEK1 interactors in response to rabusertib identified by AP-MS. Known CHEK1 interactors are highlighted with a blue border. P-values were calculated using a moderated t-test followed by multiple testing corrections using the procedure of Benjamini-Hochberg. B) GO enrichment analysis (biological process) of all interactors of CHEK1 identified by AP-MS. P-values were calculated using a Fisher's exact test followed by multiple testing corrections using the procedure of Benjamini-Hochberg. C) A highly interconnected subnetwork of the proteins associating with CHEK1 upon rabusertib treatment measured in panel A. The MCM complex is highlighted with darker edges, and known interactors of CHEK1 are highlighted with a blue border. D) Changes in the proximity of CHEK1 upon inhibition with rabusertib. P-values were calculated using a moderated t-test followed by multiple testing corrections using the procedure of Benjamini-Hochberg. E) Changes in phosphorylation upon CHEK1 inhibition with rabusertib extracted from AP-MS results. P-values were calculated using a moderated t-test followed by multiple testing corrections using the procedure of Benjamini-Hochberg. AP-MS experiments were performed in triplicates, and *in vivo* proximity labeling experiments in quadruplicates.

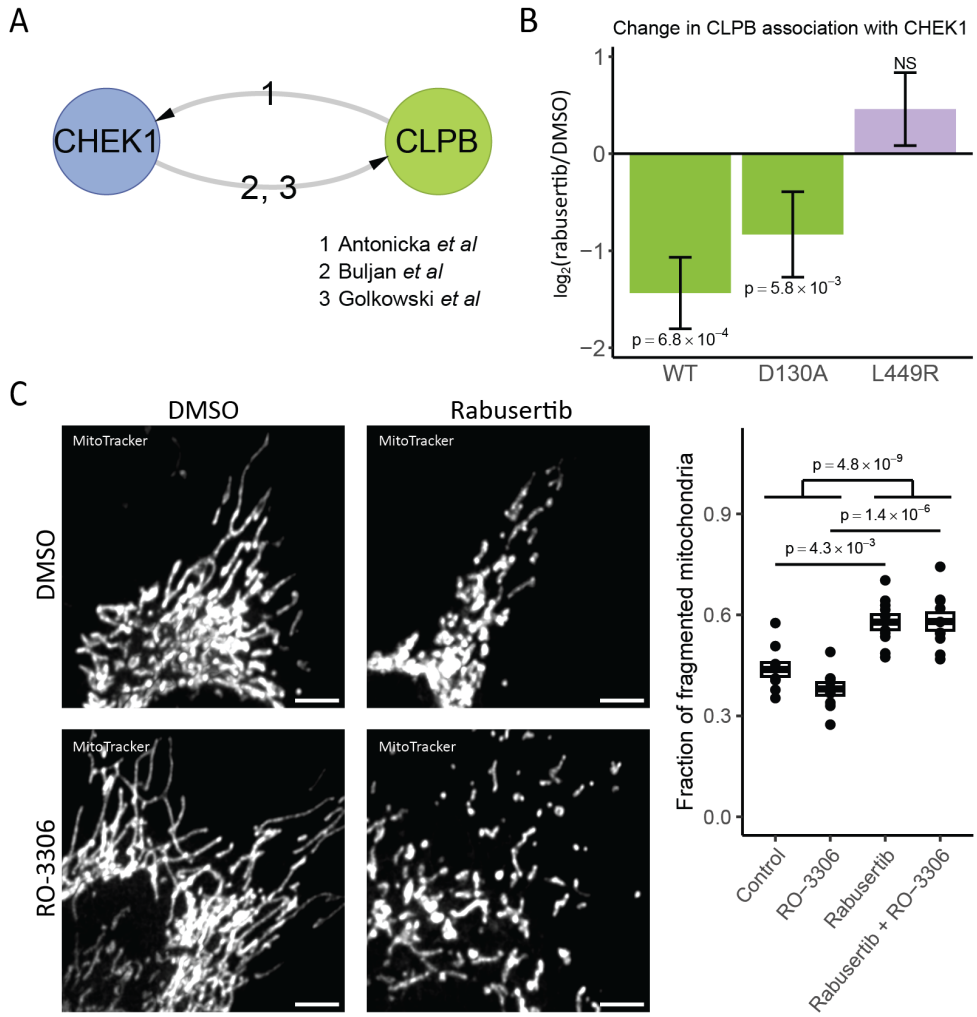

Fig. 5. Rabusertib disrupts CHEK1-CLPB complex formation and causes mitochondrial fragmentation. A) Previous studies detecting CHEK1-CLPB complex. B) Bar graph representing $\log_2$(fold change) in CLPB association with CHEK1 WT and indicated mutants upon rabusertib treatment. Error bars represent the standard error of the mean of the $\log_2$(fold change). P-values were calculated using a moderated t-test followed by multiple testing corrections using the procedure of Benjamini-Hochberg. Experiments were performed in triplicates. C) Super-resolution microscopy of mitochondria in HeLa cells treated with rabusertib in the presence and or absence of RO-3306. Images were segmented and mitochondria were classified based on their morphology as either fragmented or elongated. Within each image, the area of fragmented mitochondria was normalized by the total area of detected mitochondria. P-values were calculated by ANOVA followed by Tukey HSD. For each condition, 10 images taken across 3 replicates were quantified. The scale bars represent 5 µm.

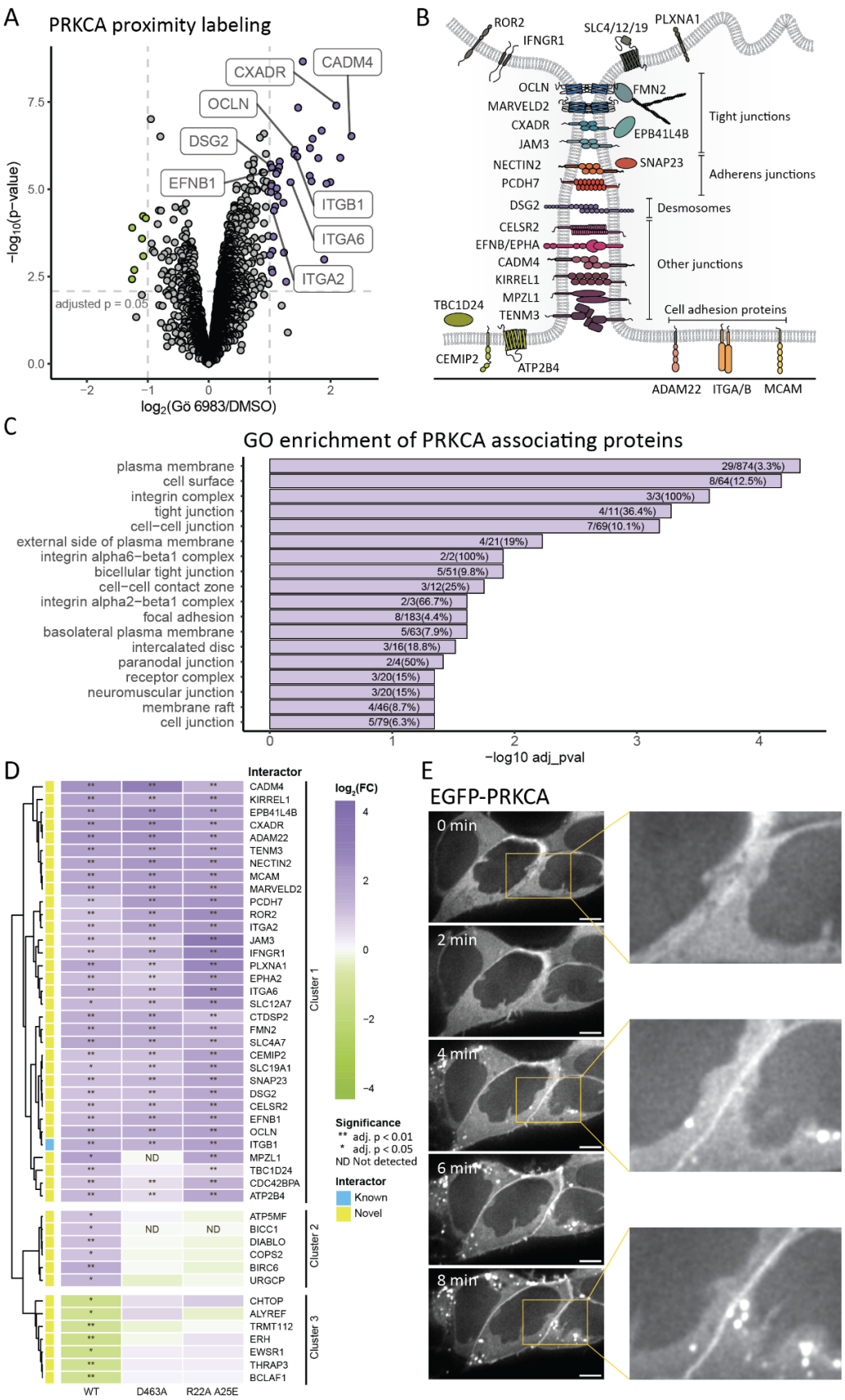

Fig. 6. PRKCA changes localization to cellular junctions upon its inhibition with Gö 6983. A) Changes in the proximity of PRKCA upon inhibition with Gö 6983. P-values were calculated using a moderated t-test followed by multiple testing corrections using the procedure of Benjamini-Hochberg. B) Illustration of the proteins annotated with GO terms 'plasma membrane' or 'cell adhesion' found increased in proximity to PRKCA upon Gö 6983 treatment. C) GO enrichment analysis (cellular component) of

proteins associating with PRKCA upon Gö 6983 treatment. P-values were calculated using a Fisher's exact test followed by multiple testing corrections using the procedure of Benjamini-Hochberg. D) Comparison of proximity changes upon Gö 6983 treatment in PRKCA WT, the catalytically inactive D463A mutant and the active R22A/A25E double mutant. P-values were calculated using a moderated t-test followed by multiple testing corrections using the procedure of Benjamini-Hochberg. E) Super-resolution live-cell microscopy of HEK293 cells expressing EGFP-PRKCA upon Gö 6983 treatment. The scale bars represent 5 μm.